Alma Mater Studiorum - Università di Bologna

SCUOLA DI SCIENZE

Dipartimento di Chimica Industriale "Toso Montanari"

Corso di Studio in

Chimica Industriale

Classe L–27– Scienze e Tecnologie Chimiche

Computational study on the asymmetric aminocatalysed Michael addition reaction of cyclohexanone to *trans*–β–nitrostyrene

CANDIDATO

Federico Lombardi

RELATORE

Chiar.mo Prof. Paolo Righi

CORRELATORE

Chiar.mo Prof. Giorgio Bencivenni

Anno Accademico 2020–2021

Abstract

Asymmetric organocatalysed reactions are one of the most fascinating synthetic strategies which one can adopt in order to induct a desired chirality into a reaction product. From all the possible practical applications of small organic molecules in catalytic reaction, amine–based catalysis has attracted a lot of attention during the past two decades. The high interest in asymmetric aminocatalytic pathways is to account to the huge variety of carbonyl compounds that can be functionalized by many different reactions of their corresponding chiral–enamine or –iminium ion as activated nucleophile and electrophile, respectively. Starting from the employment of L–Proline, many useful substrates have been proposed in order to further enhance the catalytic performances of these reaction in terms of enantiomeric excess values, yield, conversion of the substrate and turnover number. In particular, in the last decade the use of chiral and *quasi*–enantiomeric primary amine species has got a lot of attention in the field. Contemporaneously, many studies have been carried out in order to highlight the mechanism through which these kinds of substrates induct chirality into the desired products. In this scenario, computational chemistry has played a crucial role due to the possibility of simulating and studying any kind of reaction and the transition state structures involved. In the present work the transition state geometries of primary amine–catalysed Michael addition reaction of cyclohexanone to *trans*–β–nitrostyrene with different organic acid cocatalysts has been studied trough different computational techniques such as density functional theory based quantum mechanics calculation and force–field directed molecular simulations.

Summary

1. Asymmetric Synthesis

Asymmetric synthesis involves chemical reactions in which one or more new elements of chirality are formed in a substrate molecule. Moreover, enantiomeric or diastereoisomeric products are produced in unequal amounts.[1] In order to achieve asymmetric transformations, control over the three–dimensional environment in which the transformation occurs is required. If there is no stereo–directing element in place, the approach between reagents will randomly occur, meaning that both sides of the molecule will be involved in the reaction itself without a preferential pathway. In this case, a statistical mixture of the reaction products will be produced. On the contrary, the presence of a stereo–directing element favours the approach on one side of the molecule over the other. The enantioselectivity of this last process is strongly dependent on differences at the molecular level between the transition states.[2] In particular, in order to achieve stereoselectivity, energy differences of 2–3 kcal·mol^{-1} are required, which roughly equals the barrier of rotation around a single bond between carbon atoms.[2]

In conclusion, relative differences in reaction rates of the minor and major diastereomer, as well as their different equilibrium concentrations, will ultimately determine the degree of enantiomeric purity.[2]

In this first chapter, the concept of transition state will be introduced trough the transition state theory in order to highlight its chemical and physical relation with reaction products and reagents. Afterwards, the basis of asymmetric synthesis will be given followed by a small review on classical and modern strategies to obtain single enantiomers.

1.1 Transition state theory

The transition state theory has been formulated by Erying and Polanyi in 1935 in order to explain bimolecular reactions based on the relationship between kinetics and thermodynamics. This theory has been very useful tool in chemical kinetics, being very successful for parameterizing rate constants for chemical reactions with activation barriers.[3]

In the following lines, the derivation of the Eyring equation will not be rigorous. In fact, to the aim of this work, only the relation in terms of energy between the transition state and the reaction reagents and products are relevant.

It seems clear that the thoroughly comprehension of the concepts of stability and reactivity of a chemical system are required in order to understand a transformation in which it could be involved and its mechanism.[4]

The term stability is ambiguous since it is used by chemists in several senses. However, it is common to bind the concept of stability to the avoidance for chemical species to change into others[5]. It is clear that is necessary to find an unambiguous measure of stability in order to accomplish our task. Thermodynamics states that a change in a system is always accompanied by a Gibbs free energy change,[3] so the thermodynamical stability of a substance with reference to a specified transformation is quantitatively measured by this quantity.[5]

$$\Delta G^{\ominus} = \Delta H^{\ominus} - T\Delta S^{\ominus} \tag{1.1}$$

From the definition, it is evident that a variation in Gibbs free energy is always accountable to a variation in temperature, enthalpy or entropy.[3] The enthalpy change is the energy transferred as heat during an isobar transformation. Therefore, the enthalpy change gives a measure, for chemical reaction, of the difference in energy between reagents and products.[3] The entropy change, instead, is associated to a different number of the available energy levels for the species in our system, embracing the molecular interpretation given by Boltzmann: this alleges to a different probability to incur a reactive event.[3,4] The Gibbs free

energy can be expressed also as a function of the partial molar Gibbs energies of product and reagents; as these quantities change with composition, the Gibbs free energy changes accordingly, in this way, it is possible to write another formulation for the Gibbs free energy as a function of equilibrium constant K_{eq}.

$$\Delta G^{\ominus} = -RT\ ln\ K_{eq} \tag{1.2}$$

On the other hand, the term reactivity is bound to the time in which a chemical transformation occurs. This is quantitatively described by the chemical kinetics definition of reaction rate which depends on concentration and rate constant.[4]

$$v = k \prod_i C_i \tag{1.3}$$

The rate constant k, is described by Arrhenius equation as a function of the activation energy Ea and the frequency factor A: the so called Arrhenius parameters.[3]

$$k = A\ e^{-\frac{Ea}{RT}} \tag{1.4}$$

The equation 1.4 is experimentally derived from the mathematical interpretation of the trend of the rate constant against the reciprocal of temperature. In particular, in the line resulting in the abovementioned plot, the activation energy represent its slope whereas the frequency factor its intercept whit the y–axes.[3]

However, it is possible to interpretate the activation energy based on molecular considerations. As the reaction proceeds, the reactants come into a more intimate contact and their respective structures got distorted: while the distortion became more significant, the energy of the system increase. The degree of distortion keeps increasing until reaction partners begin to exchange and discard their atoms.[3] The climax of the reaction is at the peak of the potential energy, which corresponds to the activation energy.[3,4] The structure associated to the aforementioned energy maximum on passing from reagent to products is called transition state.[6]

The transition states are not real molecules rather they can be considered as species which have some common features with both the reagents and the products for what concerns their structures: they may show partial broken bonds or almost formed ones and more atoms surrounding a centre than allowed by valence bond rules. It is also important to highlight that transition states cannot be isolated due to their high energy alleging to a more stable arrangement for any change in their structures caused by *i.e.* separation processes.[6]

Now, it is clear that the nature of the rate constant is strongly related to the geometry adopted by the reaction partners at the peak in energy along the reaction coordinate; all the treatment regarding the chemical kinetics could be further expanded through the activated complex theory.[3]

The transition state theory states that the reaction partners are considered at the equilibrium with their respective transition state before they can form the products; for a bimolecular reaction, the reaction equation can be written as follows:

$$A + B \rightleftharpoons AB^{\ddagger} \rightarrow P$$

Following chemical kinetics, it is possible to write (equation 1.5a) the reaction rate equations as a function of a rate constants and the concentration C_i of the reactant involved in the two steps.

$$r_{AB^{\ddagger}} = K^{\ddagger}\, C_A\, C_B \qquad (1.5a)$$

$$r_P = \kappa\, \nu\, C_{AB^{\ddagger}} \qquad (1.5b)$$

The equation 1.5b correlates the reaction rate for the formation of the reaction product with the concentration of the transition state through its decomposition frequency ν and a factor κ which takes care of the number of collisions that results in a reactive event. The first term can be rationalized as the frequency at which the transition state overcomes the reaction energy barrier. From a molecular point of view, this is strongly bound to the frequency at which the asymmetric vibration at which new bonds are progressively formed and the old

bonds are simultaneously broken occurs. For a non–ideal system, it is possible to define the equilibrium constant for the formation of the transition state $K^{\ddagger}$ as function of concentration relative to all the species present in the system passing through activities.

$$K^{\ddagger} = \frac{a_{AB^{\ddagger}}}{a_A a_B} = \frac{\frac{C_{AB^{\ddagger}}}{C^{\ominus}}}{\frac{C_A}{C^{\ominus}}\frac{C_B}{C^{\ominus}}} = \frac{C_{AB^{\ddagger}} C^{\ominus}}{C_A C_B} \tag{1.6}$$

From this last relation, it is possible to derive an expression for the transition state concentration as a function to the reactant concentrations and the equilibrium constant for the formation of the first one.

$$r_P = \kappa\, \nu\, K^{\ddagger} \frac{C_A C_B}{C^{\ominus}} \tag{1.7}$$

Following statistical thermodynamics, it is possible to express the equilibrium constant as function of global molar partition functions for every reagent and products.

$$K^{\ddagger} = \frac{\frac{q^{\ominus}_{AB^{\ddagger}}}{N}}{\frac{q^{\ominus}_A}{N}\frac{q^{\ominus}_B}{N}}\, e^{-\frac{\Delta E}{RT}} = \frac{q^{\ominus}_{AB^{\ddagger}} N}{q^{\ominus}_A q^{\ominus}_B}\, e^{-\frac{\Delta E}{RT}} \tag{1.8}$$

The global molar partition function can be expressed for non–monoatomic and non–interacting chemical species as the product of the single translational, rotational, vibrational, electronic and nuclear molar partition functions.

$$q^{\ominus}_i = q^{\ominus}_{i,\, tras}\; q^{\ominus}_{i,\, rot}\; q^{\ominus}_{i,\, vibr}\; q^{\ominus}_{i,\, el}\; q^{\ominus}_{i,\, nucl} \tag{1.9}$$

Focusing our attention on vibration partition function, it can be expended for normal modes vibration as it follows:

$$q^{\ominus}_{i,\, vibr} = \frac{1}{1 - e^{-\frac{h\nu_i}{k_B T}}} \tag{1.10}$$

The partition function includes a factor that takes care of the vibration corresponding to the complex falling apart.

This vibration is much lower than for an ordinary molecular vibration so the partition function can considered equal to:

$$q^{\ominus}_{i,\,vibr} \approx \frac{k_B T}{h\nu_i} \tag{1.11}$$

The expression of $K^{\ddagger}$ can be then expanded as follows:

$$K^{\ddagger} = \frac{k_B T}{h\nu} N \frac{q^{\ominus}_{AB^{\ddagger},\,tras}\; q^{\ominus}_{AB^{\ddagger},\,rot}\; q^{\ominus}_{AB^{\ddagger},\,el} q^{\ominus}_{AB^{\ddagger},\,nucl}}{q^{\ominus}_{A} q^{\ominus}_{B}} e^{-\frac{\Delta E}{RT}} = \frac{k_B T}{h\nu} K^{\ddagger}_{-1} \tag{1.12}$$

The other terms of the global partition function for the transition state are not always immediate to calculate but considering $K^{\ddagger}_{-1}$ as an equilibrium constant despite one vibrational mode, it can be expanded through the equation 1.2

$$K^{\ddagger} = \frac{k_B T}{h\nu} e^{-\frac{\Delta G^{\ddagger}}{RT}} \tag{1.13}$$

In conclusion we can express the reaction rate for these kind of reaction as a function of the transition state thermodynamics quantities.

$$r_P = \kappa\nu \frac{k_B T}{h\nu}\; e^{-\frac{\Delta G^{\ddagger}}{RT}}\; \frac{C_A C_B}{C^{\ominus}} = \kappa \frac{k_B T}{h} \left(e^{-\frac{\Delta H^{\ddagger}}{RT}}\; e^{\frac{\Delta S^{\ddagger}}{R}} \right) \frac{C_A C_B}{C^{\ominus}} \tag{1.14}$$

The equation 1.13 is known as Eyring equation which is an analogous of the Arrhenius expression of the reaction rate: it is possible to demonstrate that the enthalpy change can be correlated to the activation energy and entropy change can be correlated to the frequency factor.

$$\Delta H^{\ddagger} = Ea + RT \tag{1.15a}$$

$$\Delta S^{\ddagger} = R\, ln \left(A - \frac{h}{k_B T} \right) \tag{1.15b}$$

It is now clear that Eyring equation can be used as a reaction rate equation in term of thermodynamic quantities related to the transition state of a reaction.

Eyring equation is useful to highlight the relation between the change in Gibbs free energy, relative to the formation of transition state and the activation energy of the reaction itself: any change related to the geometry of the transition state causes a variation in the Gibbs free energy and then a variation in the activation energy for the reaction. The transition state is a sort of half–way structure between the reaction partners and the product, so that any geometrical variation in one of them causes a different energy for the transition state geometry and then its energy.

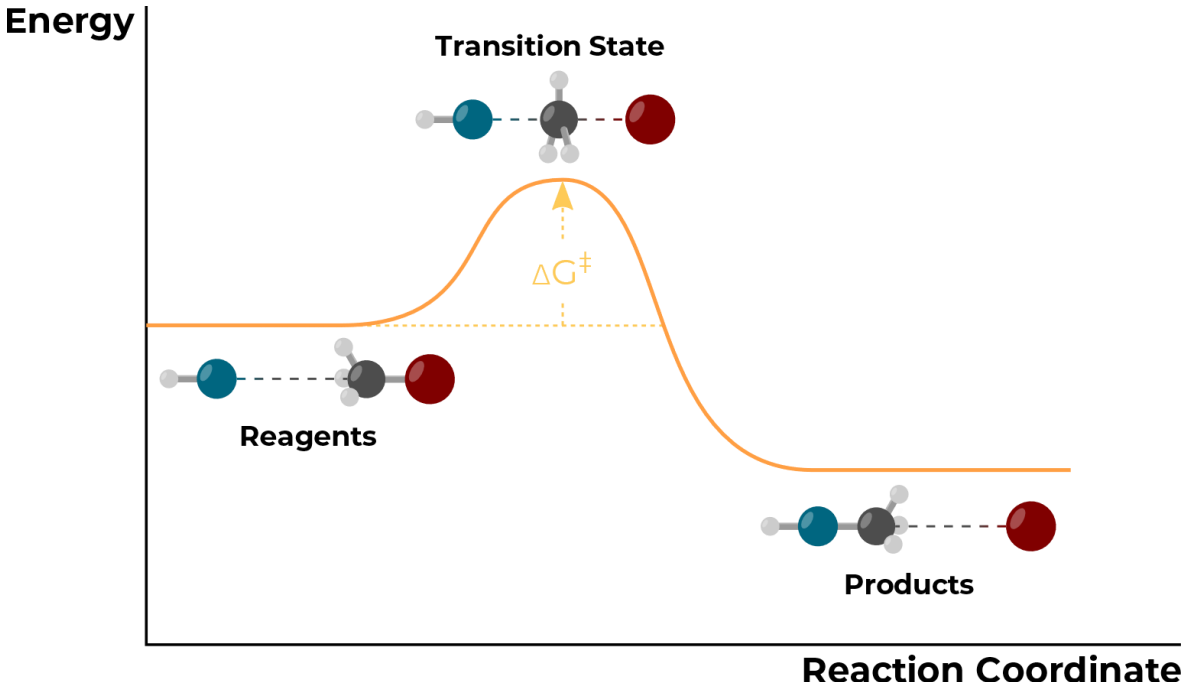

Figure 1.1. Representation of reaction pathway passing through transition state structure.

1.2 Stereoselective Synthesis

The main objective of stereoselective synthesis is to obtain a chiral product from the conversion of a prochiral precursor with the use of optical active materials.[7]

Prochirality is mandatory in order to obtain a molecule with specific chirality due to the fact that the reactions of such species generate the desired products in a single step.[6]

Prochiral molecules are achiral molecules which could generate both enantiomers and diasteroisomers as a function of the subunit surrounding their reaction centres which defines the topicity relations between them. The understanding of topicity relations between reaction centres such as faces or groups of the same molecule are fundamental in order to predict which kind of stereoisomerism relation will establish between the possible reaction product. Therefore, it is possible to discriminate among diasterotopic, enantiotopic or homotopic reaction centres analysing whether the stereochemical relation between the products obtainable is diasteromerical, enantiomerical or the products are the same molecule[6].

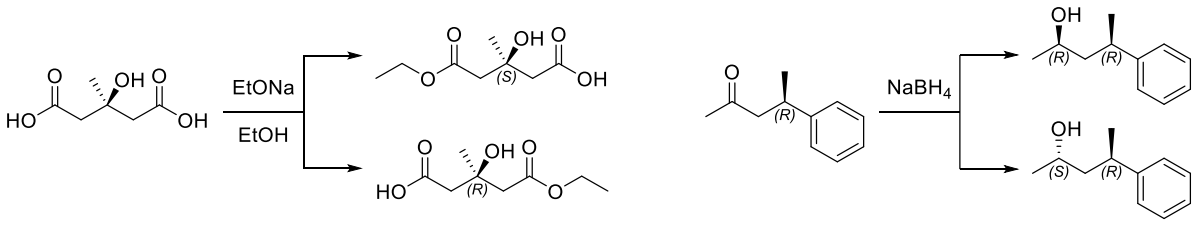

Figure 1.2. On the left, enantiotopic carboxylic moieties generate two enantiomers after esterification. On the right, diasterotopic faces of the carbonyl group generate two diasteroisomers after reduction.

When the stereochemical relation between the reaction products is known, it is possible to speculate about the stereochemical relation between transition state structures generated in the presence of an achiral reaction partner following the consideration given in the previous section.

For molecules with diasterotopic reaction centers, such as diasterotopic face, it is possible to assume that the transitions states which led to the diasteromeric products are also bound by a diasteromerical relation. This affirmation is supported by the structure of the transition state corresponding to a geometrical distortion of the reagents atoms which mime the products structure.

Diasteroisomers are chemical species which might show slight or starker differences in physical and chemical properties so that they differ also for what concerns energy in terms of thermodynamical stability and then Gibbs free energy.[6] This difference in stability is reflected on the transition states energies revealing different activation energies for different products.

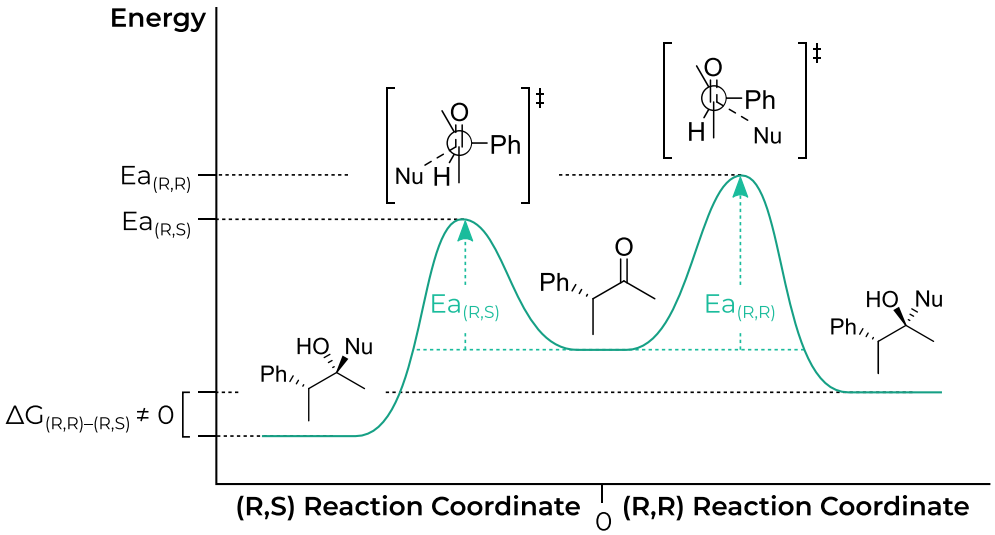

Figure 1.3. Example of transition state energies distribution for the reaction of prochiral (*R*)–3–phenylbutan–2–one and an achiral nucleophile.

On the contrary, when enantiotopic reaction centres, such as enantiotopic faces, are involved, it is possible to assume that the transitions states, which led to the enantiomeric products, are also bound by an enantiomerical relation.

In contrast to diasteroisomers, enantiomers are non–superimposable mirror images one another showing identical properties in an achiral environment. Therefore, they must also have the same thermodynamical stability[6]. As a consequence, this condition reveals the same activation energies for different stereoisomers.

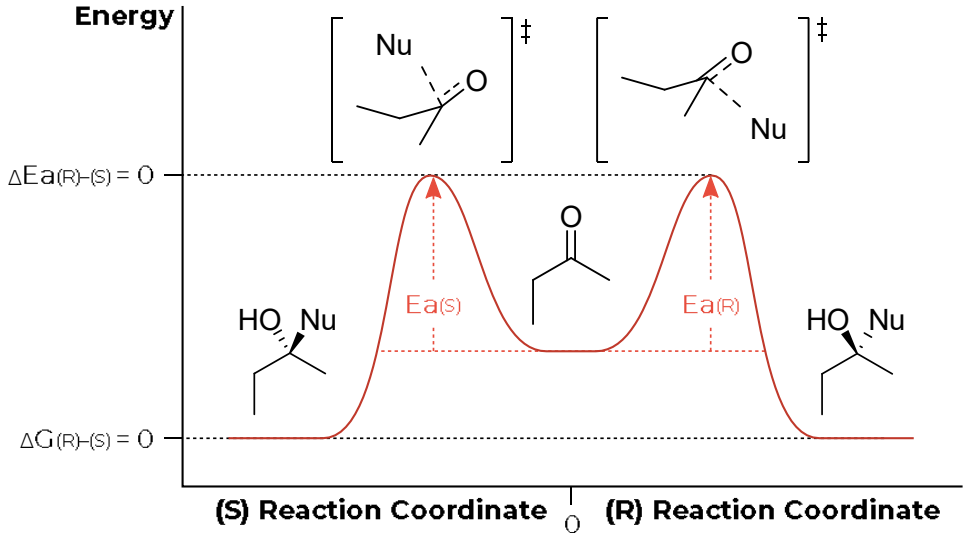

Figure 1.4. Example of transition state energies distribution for the reaction of prochiral ethyl methyl ketone and an achiral nucleophile.

This second scenario leads to the impossibility to obtain a single enantiomer from the reaction with an achrial partner with enantiotopic functional groups rather than a racemic mixture.

To overcome this problem, three main strategies have been developed in the last years for the preparation of single enantiomers[6]:

I. Resolution of the first prepared racemate mixtures by chemical or physical methods;

II. Synthesis using species from *chiral pool* substituting prochiral reagents;

III. Asymmetric synthesis.

1.2.1 Resolution of racemates

The resolution is a process in which a racemate separated into single enantiomers through physical and chemical processes by the use of a resolving agent.[6]

The classical resolution process involves a chiral enantiopure species (the resolving agent) to react with the racemic mixture to form a mixture of two diastereoisomers without affecting the chiral centres of the racemate.[6] As diasteroisomers have different physical properties, they can be separated conventional separation techniques, such as fractional crystallization, distillation, or chromatographic methods.[7]

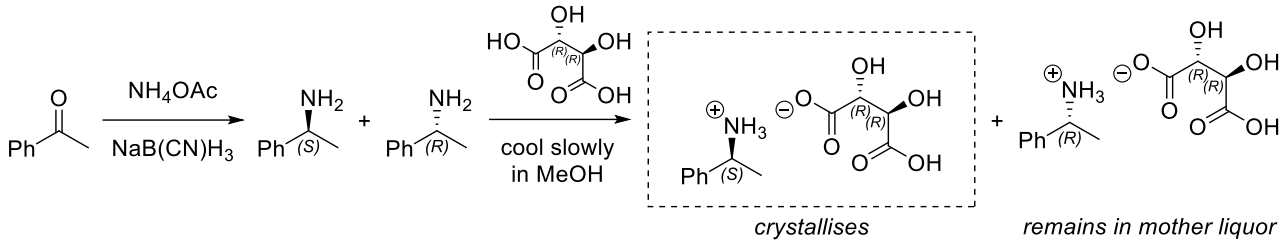

Figure 1.5. Resolution of racemate solution of 1–phenylethan–1–amine by preferential crystallization of the two diasteromeric salts obtained by reaction with (*R*,*R*)–tartaric acid.

Another resolution strategy involves chromatography with an enantiodifferentiating stationary phase; the racemates components form diasteromeric complexes by adsorption on the stationary phase which are not equally stable. Thus, the one of the two enantiomers which creates weaker interaction with such stationary phase passes through the column more rapidly.[7]

In the kinetic resolution, a single enantiomer can be obtained by reacting a racemate in a reaction that consumes one enantiomer faster than the other one. This can be achieved by using a chiral catalyst or a living system like enzyme.[6]

1.2.3 Synthesis from the *chiral pool*

The *chiral pool* is a group of enantiopure natural products which contains all the stereochemical information needed for the desired product. It is mostly constituted by natural amino acids and sugars or by substances easily derived from them.[6]

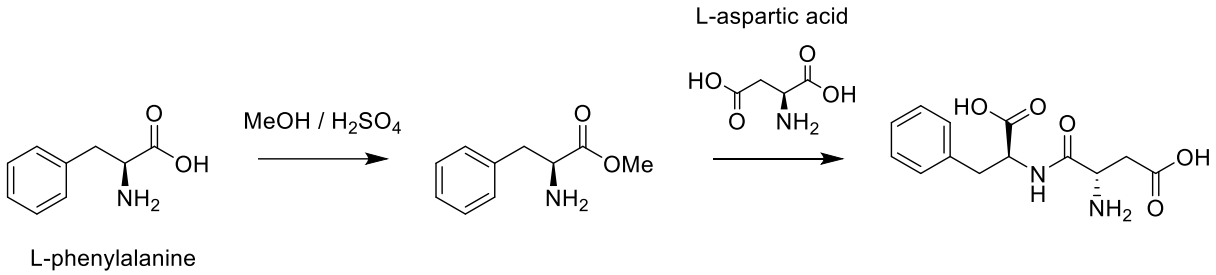

Figure 1.6. Synthesis of aspartame from natural aminoacids L–phenylalanine and L–aspartic acid.

Every reaction in which a chiral reagent is involved as starting material is highly stereospecific alleging to a complex reactions' pathways with numerous protecting and deprotecting steps. Even if the *chiral pool* is quite rich in raw materials, the only obtainable products are those who have a similar structure and chirality with the molecule selected from the *pool*. The major drawback in using natural product as carrier of the chiral information is related to the presence of only one enantiomer.[6]

1.2.4 Asymmetric synthesis

During the last couple of decades, asymmetric synthesis has made huge progresses both in the application of chiral auxiliaries and in inventing asymmetric catalytic reactions. This technique has reached an impressive degree of advancement in terms of versatility, obtainable enantiomeric excess, molar yields and turnover numbers. For these reasons, it is difficult to imagine that the asymmetric synthesis which uses small chiral homogeneous or heterogeneous catalysts is not going to become more popular than the use of enzymes and microorganisms. This is due to the fact that "living" catalysts are tuned for only one of the

two possible enantiomers of a given substrate or product, instead of the first ones which can be synthetised in order to catalyse the formation of both enantiomeric forms of the products.[7] The fundamental principle of asymmetric synthesis is differentiating the energies of two enantiomeric transition state deriving from a prochiral substrate.

The idea is to take the principle of turning a racemic mixture into a diasteroisomeric one from the resolution strategy and applying it to the transition states by binding an enantiomerically pure entity to them. This entity could be the substrate after functionalization, the reaction partner or also a catalyst[6].

1.2.4.1 Chiral auxiliaries

Chiral auxiliaries are nothing but enantiomerically pure molecules which are possible to attach onto the substrate without affecting its reactivity in the desired reaction centre. The employed auxiliary should satisfy the following requirements:

I. owing chiral information in order to be able to change the topicity of the reaction centre from enantiotopic to diaterotopic

II. to be easily removable at the end of the reaction.

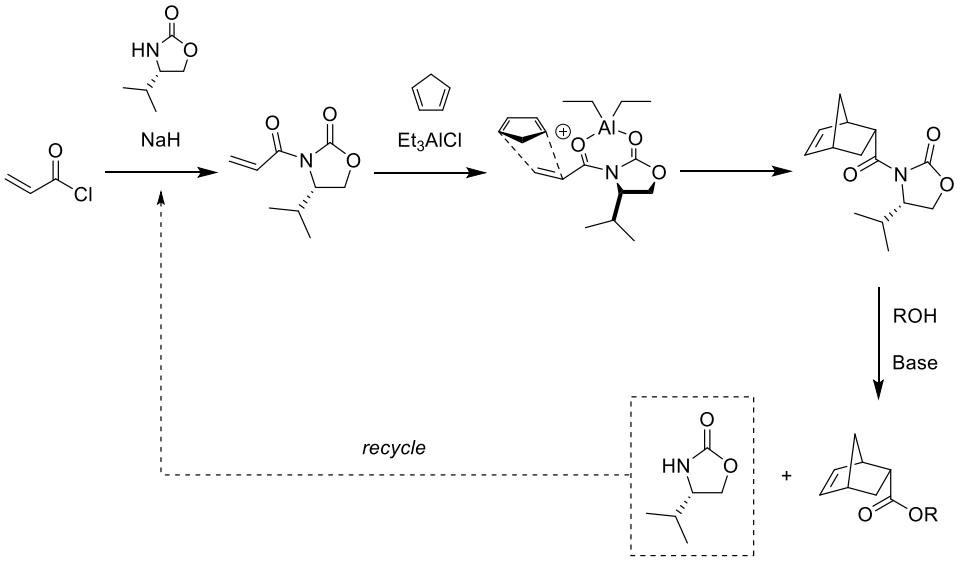

Figure 1.7. Diels–Alder reaction between cyclopentadiene and acryloyl chloride attached to a chiral auxiliary: an Evans' oxazolidinone.

The major drawback with chiral auxiliaries is the necessity to be bound to the reagents in order to induct chirality and removed afterward. These simple but unproductive steps must be included into the synthetic pathway.

1.2.4.2 Chiral reagents

Chiral reagents are the counterparty of chiral auxiliaries and they consist in enantiomerically pure molecules which are possible to covalently bond to the reaction partner. In this case, the difference in energy of the transition states is given by preferential interaction with an enantiotopic face of the prochiral substrate rather than the other. This ability is related to a different interaction of the chiral fragment with the reagent.[6]

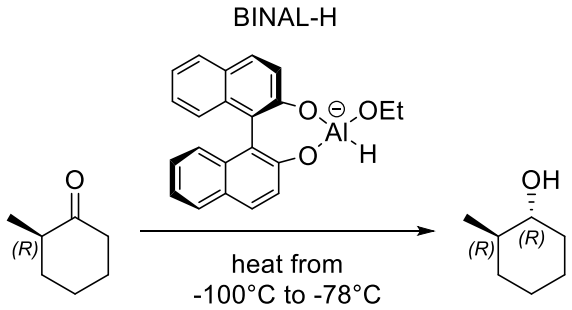

Figure 1.8 Stereoselective reduction of 2–methylchyclohexanone with an atropisomeric reducting agent.

1.2.4.3 Chiral catalysts

The chiral information responsible for the difference in energy of the transition state is given by the catalyst which can be inorganic with chiral ligands, enzymatic or even a small organic molecule: in this last case the catalysis is called asymmetric organocatalysis[6].

1.3 Asymmetric Organocatalysis

The term organocatalysis was introduced by David MacMillan[6,8] to describe the ability of small organic molecules to achieve catalytic asymmetric transformations like the metal mediated catalysis.

The organocatalysts are employed in lower amount with respect to chiral reagents but still higher than metal catalysts. Asymmetric organocatalysis is divided in two sub–classes on the basis of the strength of the bond that is established between the prochiral substrate and the catalyst[6].

I. Covalent organocatalysis;

II. Non–covalent organocatalysis.

In the first case, the catalyst is covalently bonded with the prochiral substrate with an energy associated to this of about 15 kcal·mol^{-1}. On the other hand, non–covalent organocatalysis is characterized by weaker interaction since the interaction between the partners are usually via ion pairing or hydrogen bonding with an energy lower than 4 kcal·mol^{-1}. Non–covalent catalysts are chiral organic acids or bases which induct chirality onto the substrate by creating a chiral pocket where the (de)protonated substrate has one face extremely sterically hindered.

1.3.1 Aminocatalysis

The most illustrious example of asymmetric covalent organocatalysis is the aminocatalysis for the activation of carbonyl compounds trough amines.

The origin of asymmetric aminocatalysis was established in early 2000 when L–proline was used to promote the enantioselective direct aldol reaction between a prochiral ketone and a variety of aldehydes by Benjamin List, Richard A. Lenner and Carlos F. Barbas[9]. Soon after this publication, the first aminocatalyzed asymmetric Diels–Alder reaction was carried out using a chiral imidazolidinone as catalyst demonstrating the effectiveness in the activation

of α,β–unsaturated aldehydes. In both cases, the chiral induction on the substrate is provided by the nitrogen substituents. As a consequence of the broad range of carbonyl compounds that can be functionalized trough a reaction with a simple amine, asymmetric aminocatalysis got rapidly an enormous interest especially for the effectiveness of the process and the simplicity related to the attaching and removing and therefore recycling of the catalyst[10].

The first reaction from which all aminocatalytic strategies belong is the reaction between a carbonyl compound and a secondary amine which results in the formation of an iminium ion. When this ion is formed, an equilibrium is established with the corresponding enamine.

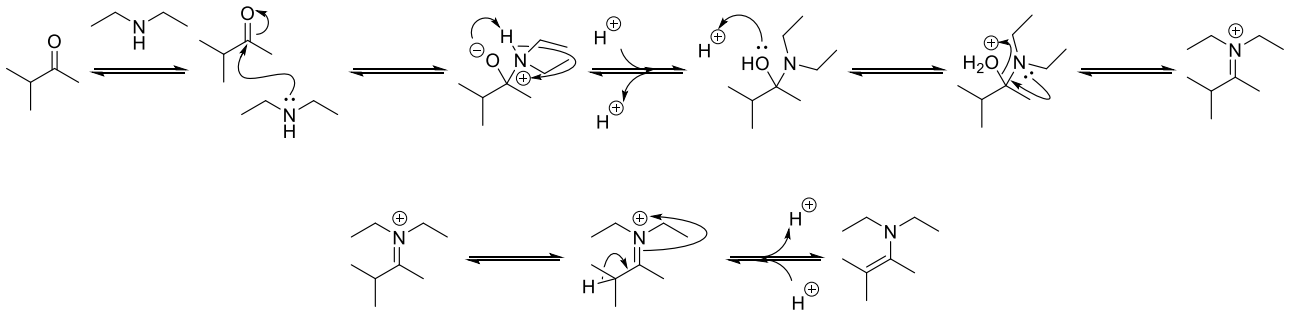

Fig. 1.9 Example of iminium ion–enamine equilibrium obtained by reaction of diethylamine and isopropyl methyl ketone.

Enamine and iminium ions are the nitrogen analogues to enol and ketones carbonyl functionality, respectively. However, the presence of the nitrogen atom instead of the oxygen atom cause an increase in reactivity in the nitrogenated analogues, in particular:

- Enamines show a more nucleophilic character on the β–carbon atom in comparison to its oxygenated analogue. This is due to the stronger conjugation of the nitrogen atom in comparison to the oxygen: the lone pair of the nitrogen atom alleges an increase in electron density on the carbon atom. As a consequence, the enamine energy of the HOMO is higher than the one of the substrate.[4,10]
- Iminium ions show, instead, a more electrophilic character on the α–carbon atom in comparison to the carbonyl compound. This is due to the decreased electron density

on the carbon atom granted by the positively charged nitrogen atom: the imine formation results in a lowering in energy of the LUMO of the substrate.[4,10]

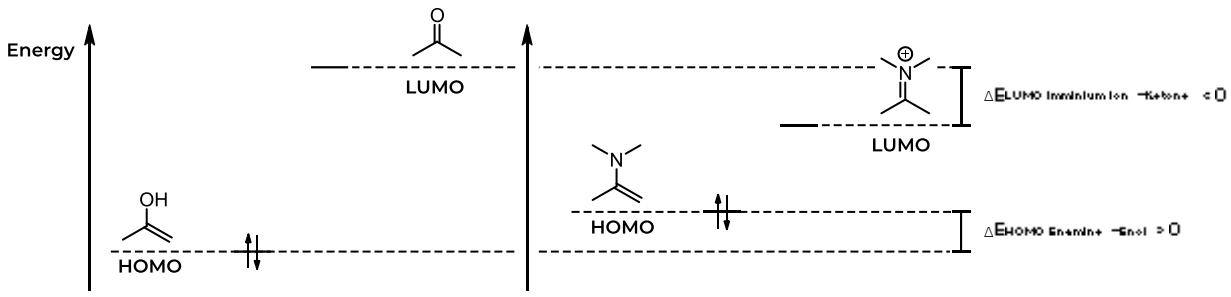

Fig. 1.10 Simple visualization of the energy gaps between both enamine and enol HOMO and iminium ion and ketone LUMO.

1.3.2 Aminocatalytic reactions mediated by L–proline

In proline catalysis, a simple natural amino acid efficiently imitates the catalytic pathway and mechanism via enamine formation[10] characteristic lyisine–based active site of type I aldolase enzymes employed by biologist.[11]

By 2000 on, proline catalysis has been extensively studied and developed with such impressive results that proline has been considered the "simplest enzyme" in nature[10]. Although the intense interest, some debate remained over the mechanism which involves the reactant during the catalytic reactions and various alternative models have been proposed during the years[11].

Hajos *et al.*[12] suggested the first two possible mechanisms which both involved the activation of one of the enantiotopic carbonyl by the reaction with the pyrrolidine nitrogen atom to form a hemiaminal in the transition state. The first transition state proposed showed the hemiaminal formed with the oxygen atom which belongs to the proline carboxylic moiety; the second one involved the hemiaminal formation with the oxygen atom which belonged to

the enantiotopic carbonyl. In the first case the enantioselectivity was justified by the hydrogen bonding between the proline hydrogen atom and the acceptor oxygen atom; in the second case, two hydrogen bonding interactions were suggested one between the proline hydrogen atom and the oxygen atom which belongs to the donor and the other between the proline carboxylic moiety hydrogen atom and the oxygen atom which forms the hemiaminal.

Fig. 1.11 Representation of the two transition states structures proposed by Hajos *et al.*[12]

Another mechanism was proposed by Agami and colleagues which involved two proline molecules: the first one has the role to form the enamine whilst the other one forms a quaternary amine by the deprotonation of the carboxylic acid of the first molecule. This allows for the establishment of a hydrogen bonding interaction between both the nitrogen atom of the first pyrrolidine and the oxygen of the carbonyl acceptor.[13]

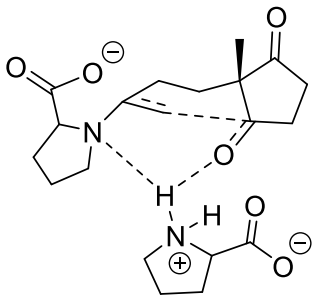

Fig. 1.12 Representation of the transition state structure proposed by Agami *et al.*[13]

Swaminathan *et al.* suggested the possibility of a heterogeneous mechanism on the surface of crystalline proline despite the fact that many proline–catalyzed aldolizations are

completely homogenous.[11] The enolization process and the chirality induction take place simultaneously on the surface of the bifunctional chiral proline crystal where the synchronous protonation of the acceptor carbonyl functionality and deprotonation in order to form the enolate are permitted by the carboxylate and the quaternary amine functionalities respectively by the proline zwitterionic form.[14]

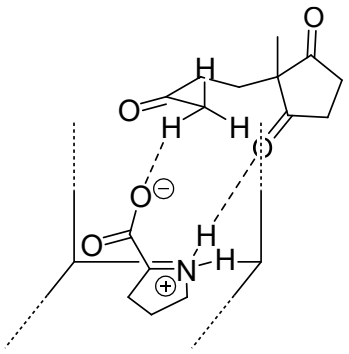

Fig. 1.13 Representation of the transition state structure proposed by Swaminathan *et al.* [14]: the reaction takes place onto the proline crystal' surface.

List *et al.*[9] proposed a mechanism for the asymmetric proline catalysis passing through a transition state in which only one molecule of proline is involved. Proline is assumed to functions as a "micro–aldolase" that provides both the nucleophilic and an acid/base cocatalyst in the form of amino group and carboxylate respectively. This cocatalyst may facilitate each individual step of the mechanism, including the nucleophilic attack of the amino group, the dehydration of intermediate to form iminium ion, all the two steps of the hydrolysis but especially the carbon–carbon bond forming step. In this scenario of one molecule transition state, the enantioselectivity is explained with a metal–free analogue of a Zimmerman–Traxler transition state. In particular, the hydrogen atom interacts with the proline nitrogen atom and both acceptor and carboxylic functionality oxygen atoms via hydrogen bonding.

The Zimmerman–Traxler transition model can be rationalized as a compact six–membered ring structure firstly suggested by di Zimmerman *et al.*[15] in the analysis of the aldol reaction

mechanism mediated by metal centres. The chair–like structure is supposed to exist thanks to the presence of the metal centre which coordinates both acceptor and donor: this coordination allows both a more intimate contact between the reaction partners and the polarization of the acceptor carbonyl. The sp^2 hybridization of the carbon atoms both of the acceptor and donor change to sp^3 while the interaction between the metal centre and the enolate oxygen atom gradually decrease in strength as the one with the acceptor oxygen atom increase, as the reaction proceeds following a pericyclic process.

In the case of proline catalysis, the hydrogen atom mimes the role of the metal centre.

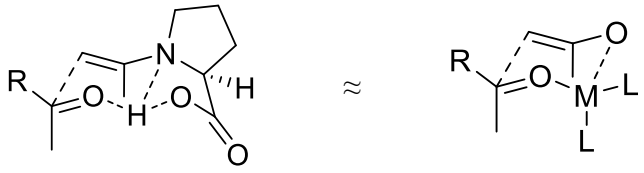

Fig. 1.14 Representation of the transition state structure proposed by List *et al* compared whit the Zimmerman–Traxler transition state model.

On the basis of density functional theory calculations, Bahmanyar *et al.*[16] broadened the transition state proposed by List and coworkers revealing that in the computed transition state geometry, the carboxylic acid proton and enamine nitrogen have a distance that does not allows the reaction partner to arrange in an ideal Zimmerman–Traxler six–membered ring as suggested by the previous studies.

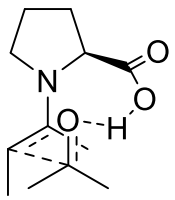

Fig. 1.15 Representation of the transition state structure proposed by Bahmanyar *et al.*[16]

The transition state geometry proposed is the more accepted by scientific community.

1.3.3 Aminocatalytic reactions mediated by primary amines

If chiral secondary amine catalysts got most of the attention in the field of asymmetric aminocatalysis, otherwise happened for chiral primary amines. Primary amine catalysis is effectively exploited by natural enzymes which contains catalytically active lysine residues[10]. The little interest in this class of amines seems to be justified since it is widely accepted that enamines formed by reaction with secondary amines are better stabilized by hyperconjugation than its counterpart obtained via primary amines[17]. Moreover, the relative high tendency of primary enamines to tautomerize causes lost in information regarding carbon double bond conformation[18]. However, the presence of a hydrogen on the nitrogen atom, rather than the alkyl group, can facilitate the effective formation of an active catalytic intermediate. In fact, in terms of catalytic efficiency for the intramolecular aldol reaction, the good experimental response has led to the development of chiral primary amines as catalysts in the last few years[17]. Primary amine catalysts can be classified in four classes:

I. Natural primary amino acids and their derivatives;

II. Chiral diamines;

III. Amino–derivative of natural Cinchona alkaloids;

IV. Primary amine catalysts containing chiral counter ions.

Inspired by the effectiveness of proline in asymmetric organocatalysis, the first attempt was to try to use other natural aminoacid to achieve similar results. Córdova *et al.*[19] disclosed that primary amino acids, such as alanine, valine, aspartate, isoleucine, and serine were excellent catalysts in direct asymmetric aldol reactions of aldehydes and various ketones alleging to enenatiomeric excess values higher than 99%. Moreover, it was demonstrated that fuctionalized aminoacids such as oxygen functionalized threonine could efficiently catalyse aldol reactions with high yields, *syn*–selectivity and high enantioselectivity after silylation or *tert*–butilation of its alcoholic moiety[17].

In 2007 the first attempt of using a primary chiral diamine as catalyst in aldol reaction was carried out: Luo *et al.*[20] reported a simple chiral primary–tertiary diamine–catalyzed derived from trans–diaminocyclohexane. It was found that such diamine effectively catalyses the abovementioned reaction affording the *syn*–aldol products with excellent enantioselectivity and diastereoselectivity. They suggested that the *syn*–diastereoselectivity could be explained by the role of the tertiary amine as a directing group through the hydrogen bonding interaction with aldehyde substrates. In the following years, lots of chiral diamine catalyst were developed starting from the *trans*–diaminocyclohexane fragment. In particular, Yalalov *et al.*[21] developed a mono–functionalized *trans*–diaminocyclohexane with a thioureic fragment with a chiral centre. For the first time a chiral primary amine–thiourea organocatalyst was successfully applied successfully to an asymmetric Mannich reaction with high yields and excellent enantiomeric excess values. It was found that the use of the easily accessible bifunctional primary amine–thiourea catalysts favours the complexation via hydrogen bonding of the enol form of the ketone over the formation of the enamine. This observation expands the mechanistic paradigm of enamine aminocatalysis introducing an amine–thiourea catalysis which stabilize the enol tautomer of the ketone through week bonding interaction. Simultaneously, McCooney and Connon[22] employed inexpensive and available in both pseudoenantiomeric natural Cinchona alkaloids amino–derivatives in order to demonstrate their organocatalytic effectiveness. The tunability of these substrates for what concern the chiral environment through the inversion of configuration of the carbon atom carrying the chiral amine together with the possibility of design both primary and secondary prototype amine catalysts affords an exceptional degree of scope for catalyst optimization from these simple starting materials. McCooney *et al.* exploited the amino–derivative of Cinchona alkaloids in nitro–Michael processes with both different nitro alkanes and carbonylic substrates achieving high *syn*–selectivity in the addition reactions of enolizable carbonyl compounds to nitroolefins with relatively low catalytic loadings. Zhou *et al.*[23] analysed the catalytic efficiency, in terms of enantiomeric ratio of different primary amines as catalysts for intramolecular aldolization. The reaction was conducted with both

chiral and achiral amines leading to different results, in particular the use of derivatives of natural cinchona alkaloids in combination with different acidic cocatalysts gave the best results. The use of quinidine or cinchonine in combination with different acid in various molar ratio, proved to be efficient and highly enantioselective catalysts for intramolecular aldolization giving high enantiomeric ratio values. Lu *et al.*[24] applied the amine derivative of natural Cinchona alkaloids in an aminocatalysed aza–Michael reaction with a broad range of alkyl vinyl ketones bearing both aryl and alkyl β–substituents affording both high conversion of the raw materials and enantioselectivity. In the light of the above discussion, it is clear that asymmetric organocatalysis is one of the most useful strategies to induct chirality into prochiral substrate in order to obtain single enantiomers. As stated in the previous paragraph, this is due the wide range of reaction which can be catalysed with these species like aldol reaction and Michael Addiction to form bonds both between carbon atoms and between carbon and heteroatomic atoms like nitrogen, oxygen and sulphur and pericyclic reactions. Moreover, the loading of the chiral partner is evidently lower in comparison with asymmetric synthesis which employ chiral regents or chiral auxiliaries. Asymmetric aminocatalysis is clearly one of the most interesting and promising catalytic pathways proposed in the last twenty years: the impressive advances in primary amine catalysed enantioselective reactions have demonstrated an extraordinary usefulness and versatility of primary amines in asymmetric synthesis, establishing them as privileged catalysts in modern organocatalysis. The explosive interest on this novel class of amines as catalysts and new reaction types certainly out–paced the mechanistic understanding of these reactions. Although, the elucidation of the mechanisms of primary amine–catalysed reactions trough theoretical studies have a lot of interest not only in order to highlight the role of every single reactive species but also to improve the design of new catalysts and reactions.

1.4 References

1. McNaught, A. & Wilkinson, A. *Compendium of Chemical Terminology.* (2019). doi:10.1002/9783527626854.ch7.

2. Federsel, H. J. Asymmetry on large scale: The roadmap to stereoselective processes. *Nat. Rev. Drug Discov.* 4, 685–697 (2005).

3. Atkins, P. & De Paula, J. *Physical Chemistry Ninth Edition.* (2010).

4. Carey, F. A. & Sundberg, R. J. *Advanced Organic Chemistry Fifth Edition, Part A: Structure and Mechanisms.* (2008). doi:10.1039/9781788015097–00220.

5. Hildebrand, J. H. Factors Determining Chemical Stability. *Chem. Rev.* 2, 395–417 (1926).

6. Clayden, J., Greeves, N. & Warren, W. *Organic Chemistry Second Edition. Journal of the American Chemical Society* vol. 85 (1963).

7. Kuhlmann, J. & Puls, W. *Handbook of Experimental Pharmacology Volume 119– Oral Antidiabetics.* vol. 130 (1996).

8. Ahrendt, K. A., Borths, C. J. & MacMillan, D. W. C. New strategies for organic catalysis: The first highly enantioselective organocatalytic diels – Alder reaction. *J. Am. Chem. Soc.* 122, 4243–4244 (2000).

9. List, B., Lerner, R. A. & Barbas, C. F. Proline–catalyzed direct asymmetric aldol reactions. *J. Am. Chem. Soc.* 122, 2395–2396 (2000).

10. Melchiorre, P., Marigo, M., Carlone, A. & Bartoli, G. Asymmetric aminocatalysis – Gold rush in organic chemistry. *Angew. Chemie – Int. Ed.* 47, 6138–6171 (2008).

11. List, B., Hoang, L. & Martin, H. J. New mechanistic studies on the proline–catalyzed aldol reaction. *Proc. Natl. Acad. Sci. U. S. A.* 101, 5839–5842 (2004).

12. Hajos, Z. G. & Parrish, D. R. Asymmetric Synthesis of Bicyclic Intermediates of Natural product chemistry. *J. Org. Chem.* 39, 1615–1621 (1974).

13. Puchot, C. *et al.* Nonlinear Effects in Asymmetric Synthesis. Examples in Asymmetric Oxidations and Aldolization Reactions. *J. Am. Chem. Soc.* 108, 2353–2357 (1986).

14. Rajagopal, D., Moni, M. S., Subramanian, S. & Swaminathan, S. Proline mediated asymmetric ketol cyclization: A template reaction. *Tetrahedron Asymmetry* 10, 1631–1634 (1999).

15. Zimmerman, H. E. & Traxler, M. D. The Stereochemistry of the Ivanov and Reformatsky Reactions. I. *J. Am. Chem. Soc.* 79, 1920–1923 (1957).

16. Bahmanyar, S., Houk, K. N., Martin, H. J. & List, B. Quantum mechanical predictions of the stereoselectivities of proline–catalyzed asymmetric intermolecular aldol reactions. *J. Am. Chem. Soc.* 125, 2475–2479 (2003).

17. Xu, L. W., Luo, J. & Lu, Y. Asymmetric catalysis with chiral primary amine–based organocatalysts. *Chem. Commun.* 1807–1821 (2009) doi:10.1039/b821070e.

18. Clark, R. A. & Parker, D. C. Imine–Enamine Tautomerism. I. 2– (N–Cyclohexylimino) –1,3–diphenylpropane. *J. Am. Chem. Soc.* 93, 7257–7261 (1971).

19. Córdova, A. *et al.* Acyclic amino acid–catalyzed direct asymmetric aldol reactions: Alanine, the simplest stereoselective organocatalyst. *Chem. Commun.* 3586–3588 (2005) doi:10.1039/b507968n.

20. Luo, S., Xu, H., Li, J., Zhang, L. & Cheng, J. A Simple Primary−Tertiary Diamine−Brønsted Acid Catalyst for Asymmetric Direct Aldol Reactions of Linear Aliphatic Ketones. *J. Am. Chem. Soc.* 129, 3074–3075 (2007).

21. Yalalov, D. A., Tsogoeva, S. B., Shubina, T. E., Martynova, I. M. & Clark, T. Evidence for an enol mechanism in a highly enantioselective Mannich–type reaction catalyzed by primary amine–thiourea. *Angew. Chemie – Int. Ed.* 47, 6624–6628 (2008).

22. McCooey, S. H. & Connon, S. J. Readily accessible 9–epi–amino cinchona alkaloid derivatives promote efficient, highly enantioselective additions of aldehydes and ketones to nitroolefins. *Org. Lett.* 9, 599–602 (2007).

23. Zhou, J., Wakchaure, V., Kraft, P. & List, B. Primary–amine–catalyzed enantioselective intramolecular aldolizations. *Angew. Chemie – Int. Ed.* 47, 7656–7658 (2008).

24. Lu, X. & Deng, L. Asymmetric aza–Michael reactions of α,β–unsaturated ketones with bifunctional organic catalysts. *Angew. Chemie – Int. Ed.* 47, 7710–7713 (2008).

2. Computational Chemistry

Since the advent of electronic computers in the past century, computation has played a key role in chemistry development. Numerical methods for computing static and dynamic properties of chemicals have revolutionized chemistry.[1]

In this scenario, we have assisted to the born of a new discipline: computational chemistry. Computational chemistry includes the entire range of computational techniques that are applied to study chemical systems, whether their roots lie in physics–e.g., quantum mechanics, statistical mechanics–mathematics, informatics and/or other underlying scientific disciplines. Such techniques are extremely powerful because they allow for the prediction of molecular properties, the elucidation of unclear experimental data, and the modelling the short–lived, unstable intermediates and transition states which are impossible to observe directly.[2]

Quantum chemistry, instead, is a more specific term which refers to methods that were derived from the basic laws of quantum mechanics.

The main goal for a whole quantum mechanics–based computation technique is to associate an energy value with a particular distribution of N electrons around M nuclei in particular positions using the Schrödinger equation.[2]

$$\hat{H}\ \Psi\left(\vec{r}_1, \vec{r}_2, \ldots, \vec{r}_N, \vec{R}_1, \vec{R}_2, \ldots, \vec{R}_M\right) = E\ \Psi\left(\vec{r}_1, \vec{r}_2, \ldots, \vec{r}_N, \vec{R}_1, \vec{R}_2, \ldots, \vec{R}_M\right) \quad (2.1)$$

The Schrödinger equation correlates the wave function to an energy by a function in which the Hamiltonian operator acts on the wave function itself. The Hamiltonian operator can be expanded in all its component for a system of nuclei and electrons in atomic notation.

$$\hat{H} = -\frac{1}{2}\sum_{i=1}^{n}\nabla_i^2 - \frac{1}{2}\sum_{A=1}^{M}\nabla_i^2 - \sum_{i=1}^{n}\sum_{A=1}^{M}\frac{Z_A}{r_{i,A}} + \sum_{i=1}^{n}\sum_{j>i}^{N}\frac{1}{r_{i,j}} + \sum_{A=1}^{A}\sum_{B>A}^{N}\frac{Z_A Z_B}{r_{A,B}} \quad (2.2)$$

From the formulation of the Hamiltonian operator, it is clear that solving this equation its quite challenging. In 1927, Max Born and J. Robert Oppenheimer showed that the nuclei in a molecule are stationary with respect to the electrons to a very good approximation. This simple consideration allows the separation of the Schrödinger equation for a molecule into an electronic and a nuclear equation. Reformulating what stated some lines above, the primary goal for this kind of quantum chemical computation technique is to associate an electronic energy to and electronic wave function solving the Born–Oppenheimer approximated Schrödinger equation.

$$\hat{H}^{elec}\ \Psi^{elec}\left(\vec{r_1}, \vec{r_2}, \ldots, \vec{r_N}\right) = E^{elec}\ \Psi^{elec}\left(\vec{r_1}, \vec{r_2}, \ldots, \vec{r_N}\right) \tag{2.3}$$

In this scenario, the overall energy of the target system is computed by summing the electronic energy derived from the above equation and the nuclear energy deriving from the second and the fifth term of the equation 2.2. The Hamiltonian operator exploited in the Born–Oppenheimer approximated Schrödinger equation does not have any nuclear–only energy term.

2.1 Potential Energy Surfaces

In a three–dimensional space, all the atoms N which form a molecule can move and rotate along x, y and z cartesian axes each. This alleges to a 3N – 6 ways in which any nucleus can move in respect to another one.[3]

The potential energy surface is a hypersurface which describes how the electronic energy associated to a molecule changes accordingly to modification in its geometry. The electronic energy is the energy of nuclei and electrons arranged in a specific structure in comparison to the energy of all its constituting atoms at infinite separation.[3]

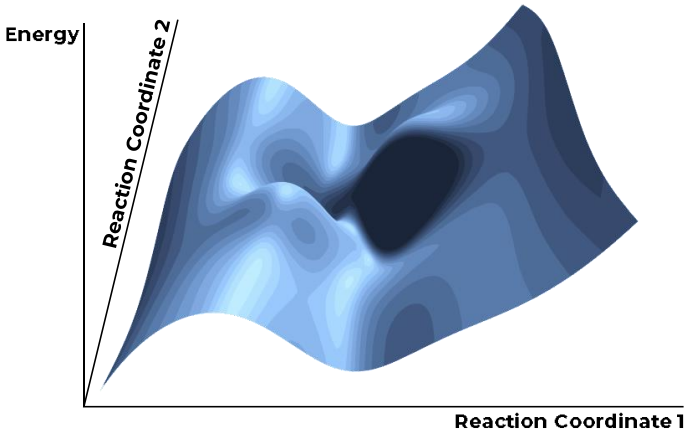

Fig. 2.1 Example of a potential energy surface.

Potential energy surfaces are characterized by the presence of critical points, also called stationary points. Critical points are points on the hypersurface which correspond to zero values in first– or second–order derivative of the energy with respect to the nuclei position.

$$\frac{dE}{dr} = \nabla \tag{2.4a}$$

$$\frac{d^2E}{dr^2} = \nabla^2 \tag{2.4b}$$

In this scenario, three possible stationary point can be encountered, in particular:[4]

- Zero value for first–order derivative and all–negative value for second order derivative correspond to a maximum.
- Zero value for first–order derivative and all–positive value for second order derivative correspond to a minimum.
- Zero value for first–order derivative and both negative and positive value for second order derivative correspond to saddle point which order is defined by the number of negative values.

Maximum points represent the highest nuclei disposition in term of energy. On the other hand, minimum points represent lowest energies nuclei dispositions while saddle points represent transition states. For a first–order saddle point, the single negative value represents the only direction following which it is possible to overcome a maximum. Thus, it represents the energetically favoured pathway from two minimum separated by the saddle point.[4]

2.2 Conformational space analysis

The research of the accessible conformations which populate the global minimum of the potential energy surface is necessary to study transformations which involves flexible molecules such as organic molecules.[3]

The majority of the approaches to the conformational search have a common starting point which is a starting geometry of the molecules.[5] As the first "crude" molecular geometry is known, the conformational search could be carried out with two main different strategies:

- All the conformational space is systematically covered by fixed increments of all or only some of the torsional angles in the selected geometry: this approach to the conformational search is called systematic or grid research.

  Through the systematic research, the coverage of all the potential energy surface is guaranteed if all dihedral angles are involved, yielding in a broad number of starting conformations. However, to achieve the complete exploration of all the available conformational space the fixed increment has to be chosen not too small in value.[5]
- The conformational space is analysed by pseudo–random variation of the internal coordinates of selected geometry: this approach to the conformational search is called stochastic or Monte Carlo research.

  On the other hand, through Monte Carlo researches the exploration of the potential energy surface is granted by random variation of torsional angle each calculation step by at least 3.5 Å. The pseudo–randomicity definition is due to the limited values of modification in the internal coordinates allowed by the algorithm. The longer the calculation time, the highest the conformational space can be considered explored, however the number of new conformers discovered decrease during the simulation.[5]

Once new conformation is discovered by one of the two abovementioned research technique, an energy minimization of the structure occurs based on molecular mechanics force field.[3]

2.2.1 Molecular mechanics

The molecular mechanics approach treats molecules as charged particles held together by simple harmonic forces.[6] The force fields are sets constituted by Newtonian equations and empirical coefficient to evaluate the properties associated to a molecular geometry in a classical way.[3] The molecular mechanics method is empirical by definition, hence all the equations and parameters are written *ad hoc* in order to better predict experimental results. For this reason, experimental results are also required and their parametrization for specific classes of atoms and bonds are mandatory to formulate all the components of any force field.[3] A broad number of force fields have been developed over the years by researchers with the aim to exhaustively foresee the properties of specific class of molecule and compounds. Even if they could be very dissimilar for what concerns parameter values and equations formalism, all force fields share the logic at the base of the evaluation of the overall potential energy characteristic of a single molecule. This is treated as the sum of both intramolecular and intermolecular interactions.[7]

$$U = U_{intra} + U_{inter} \tag{2.5}$$

The expression of these two contributes to the overall potential energy change in different force fields. The following treatment is related to the OPLS3e force field developed by Harder[8] and co–workers in 2019.

$$U = U_{stretching} + U_{bending} + U_{torsion} + U_{non-bonding} \tag{2.6}$$

All the potential energy contributes are sum over all bonds, angles, dihedral and non–bonding interactions.

The contribute to the overall potential energy of the bond stretching must depend on the nature of the bond itself in the sense of which kind of atoms are located at its extremity and their hybridization.

$$U_{stretching} = \sum_{bonds} K_r (r - r_{eq})^2 \tag{2.7}$$

The abovementioned dependency is taken into consideration in the formula by the stretch constants K_r and the equilibrium length r_{eq} of the bond. It is possible to arise analogous considerations for what concerns the contributes of angles bending.

$$U_{bending} = \sum_{angles} K_\theta (\theta - \theta_{eq})^2 \tag{2.8}$$

The potential energy associated to dihedral torsion is analogous to the previous two expressions with the exception for the presence of a truncated Fourier series in which the torsional parameters V_n appears.

$$U_{torsional} = \sum_{dihedrals} \sum_{n=1}^{4} \frac{V_n}{2} (1 + cos(n\ \phi)) \tag{2.9}$$

The non–bonding interactions contributes to the overall potential energy are represented by the sum over Coulomb and Lennard–Jones pairwise potential terms between the i^{th} and j^{th} atom.

$$U_{non-bonding} = \sum_{i<j} \left(\frac{q_i\, q_j\, e^2}{r_{ij}} + 4\, \varepsilon_{ij} \left(\frac{\sigma_{ij}^{12}}{r_{ij}^{12}} - \frac{\sigma_{ij}^{6}}{r_{ij}^{6}} \right) \right) f_{ij} \tag{2.10}$$

The electrostatic repulsion is taken into consideration by the classical Coulombian pairwise potential based on the distance between two non–bonded atom and their nuclear charges.

The Van der Waals week interactions are calculated through the Lennard–Jones pairwise potential expression. This expression takes into consideration dispersing attractive interaction generated by temporary dipoles which decays, as London suggested proportional to $-r_{ij}^{-6}$. On the other hand, the repulsive interactions generated from overlap of highlighted atoms' electron clouds is supposed to decay more rapidly, proportionally to r_{ij}^{-12} .[9] The whole non–bonding potential energy is scaled f_{ij} for atoms which are separated by three bonds or less.[8]

The overall energy associated to a specific conformation is then minimized by minimazing all the single energy–contribution trough different algorithms. The minimization algoritm, which can be derivative or not, runs until the outcome overall energy from the last step differs from the previous one by less than a specific treshold value: at this point, the structure can be considered optimized.[3]

Once the population of optimized conformers is obtained, usually an analysis of the structure occurs in order to remove the redunding conformation. This analysis is based on the calculation of the quadratic mean of the overall bonds, angle and dihedrals between two structures: if this value is under a specified treshold the two structure are considered not redundand otherwise they are considered the same structure and one of them is removed.[3]

2.3 Quantum mechanics

As suggested by the introduction of this chapter, the wave function Ψ was the central quantity exploited approaching quantum chemistry. Following to the Born interpretation, the wave function itself is a probability amplitude without a direct physical meaning which give rise to the probability of finding a particle in a volume element. Hence, once at least a good approximation the wave function is known it is possible to achieve all the information about particular states of our target system.[10] However, the electronic wave function is a very complicated quantity which depends on three spatial coordinates and one spin variable for each of the N electrons and above all, it cannot be experimentally derived. The Hatree–Fock representation of the wave function, passing through the Slater determinant of one–electron spin–orbitals, was correct since the Hamiltonian operator depends on position and atomic numbers of nuclei and on the number of electrons. However, the approximation of the electron–electron potential with a mean Coulombic repulsion alleges to the uncorrelated movement of unlike spin electrons.[10,11] The Hamiltonian operator dependency on the electron numbers suggested the exploiting of the electron density instead of the wave function for the resolution of the Schrödinger equation. The electron density is an experimentally measurable quantity and since integrated over the space it gives the total number of electrons in the target system.[10]

$$N = \int \rho(r) dr \tag{2.11}$$

Moreover, the electron density shows both non–negative values and local maxima in the position corresponding to where the nuclei are. This is due to the fact that nuclei are effectively point charges which exert an attractive force on the electrons causing high electron density values, which have cusp properties, in their proximity. Thus, it is clear that the electron density contains not also all the information about the number of electrons but also the information about the nuclei position and charges. In 1964 the founding pillars of density functional theory were erected by Pierre Hohenberg and Walter Kohn[12] with their two

theorems. The first theorem consists in a proof of existence carried out through a *reductio ad absurdum* which demonstrates that the overall electronic energy is a function of the electron density. In other words, the electron density completely describes the Hamiltonian operator. Thus, it is reasonable to affirm that all individual component of the Hamiltonian operator must be functional of the same electron density.[12]

$$E_0[\rho_0] = T[\rho_0] + E_{e-e}[\rho_0] + E_{n-e}[\rho_0] \tag{2.12}$$

It is now clear that the electron density can define all the properties of target system ground state and the second theorem of Hohenberg and Kohn describes how to find the ground electron density value. In this scenario, Hohenberg and Kohn defined the sum of the first two term as universal function which value is unique for all system. The universal functional and the system–dependent nuclei–electron repulsion energy functional $E_{n-e}[\rho_0]$ give rise to the energy value associated to the electron density under evaluation. The only possible case in which this energy corresponds to the real ground state energy is when the electron density under examination is the real ground state electron density. It is clear that the second theorem is nothing but the wave function variational principle analogue for the electron density. This theorem does not afford any simplification since the main difficult related to the expression of the electron–electron interaction term in the correct Hamiltonian is yet to overcome.[10]

Walter Kohn and Lu Jeu Sham[13] proposed to take as a starting point a fictitious system of non–interacting electrons with the electron density value equal to a real system in which electrons interact. This is possible only if the fictitious system and the real system share both the same number of electrons and the number of atom and their respective charges.[10] The overall electron energy functional correspond to the sum of the kinetic energy of the non–interacting electrons $T_{ni}[\rho(r)]$, the interaction between nuclei and electrons, the classical electron–electron repulsion $J[\rho(r)]$ and the exchange–correlation functional. This last term contains all the information regarding the non–classical electron–electron repulsion and the correction to the kinetic energy due to the interactions between electrons.[13]

$$E[\rho(r)] = E_{n-e}[\rho(r)] + T_{ni}[\rho(r)] + J[\rho(r)] + E_{XC}[\rho(r)] \tag{2.13}$$

The most of the functional in the Kohn–Sham equation are known since they derive from one–electron interaction. On the other hand, the form of exchange–correlation energy functional $E_{XC}[\rho(r)]$ lays completely in the dark, thus, the challenge is to find the best approximation the form for this functional. Since the system is considered composed by non–interacting electrons, the Hamiltonian operator is a simple sum of one electron operator called Kohn–Sham orbitals φ_i. In this scenario, must exist a Kohn–Sham operator analogous to the Fock operator.[10]

$$\hat{h}_{KS}\,\varphi_i = \varepsilon_i\,\varphi_i \tag{2.14}$$

The implementation of density functional theory depends on various *ad hoc* representation of the exchange–correlation functional and the research for more accurate functionals is an active area of current research efforts. This functional is often separated into an exchange functional and a correlation functional.[10]

2.3.2.1 Local density approximation

The local density approximation model is based on the idea of a hypothetical uniform gas of electrons which moves on a positive background charge distribution such that the total ensemble is electrically neutral. It is clear that the model is pretty far from any realistic situation in atoms or molecules, which are usually characterized by rapidly varying densities. On the other hand, the electron uniform gas is the only system for which we know the form of the exchange and correlation energy functionals with very high accuracy, so this is mainly the reason because this model is relevant.[10] The basic assumption of the model is that exchange–correlation energy per–particle is weighted with the probability that there is in fact an electron at this position in space.

$$E_{XC}^{LDA}[\rho(r)] = \int \rho(r)\varepsilon_{XC}(\rho(r))dr \tag{2.15}$$

This quantity is characterized by the sum of both exchange and correlation energies. The formulation for the exchange energy for a uniform electron gas is known under the name of Slater exchange energy. The correlation energy was highly accurate simulated trough Monte–Carlo numerical calculation even if an explicit formulation is today unknown. This model can be improved by the introduction of the spin term which is absent in the first formulation of the exchange energy: this alleges to the Local spin density approximation.[10]

2.3.2.2 Generalized gradient approximation

The generalized gradient approximation model suggests the use of the gradient of the charge density together with the electron density of the uniform electron gas in order to account the inhomogeneity of the electron density. The model exploits the local density approximation coupled with the first derivative of the electron density with respect to the spatial coordinates. The use of this Taylor–like equation allows the representation of the local non–homogeneous electron gas. The exchange–correlation energy can be divided in the two contribution of exchange energy and correlation energy. It sems clear that the exchange energy functional is a sum of the exchange–correlation energy derived from the local density approximation and an expression for the electron density gradient which takes care of the spin component σ.[10,14]

$$E_X^{GGA} = E_X^{LDA} - \beta \sum_{\sigma} \frac{|\nabla \rho_\sigma|^2}{(\rho_\sigma)^{\frac{4}{3}}} \, d^3r \tag{2.16}$$

2.3.2.3 Hybrid functionals

The Hellmann–Feynman theorem show that the exchange–correlation energy can be truly computed as a function of a parameter which describe di extent of interelectronic interaction. This parameter can range from zero to one as the system can be formed by non–interacting or fully–interacting electrons respectively.[15]

$$E_{XC} = \int_0^1 \langle \Psi(\lambda) | V_{XC} | \Psi(\lambda) \rangle \, d\lambda \tag{2.17}$$

For the non–interacting system, it is known form the Hartree–Fock approximation that the exact wave function for the Hamiltonian operator of such a system consist in the Slater determinant of one–electron functions. Thus, the exchange–correlation value corresponds to the exchange potential computed just as it is in Hartree–Fock calculations except that the Kohn–Sham orbitals are used.[15]

On the other hand, the problem of evaluating the exchange–correlation energy for the fully–interacting system still remains. However, Becke[16] proposed to approximate the total exchange correlation energy as a half–and–half contribution of the exchange energy calculated in the Hartree–Fock fashion and the exchange–correlation term deriving from the local spin density approximation.

$$E_{XC} \simeq 0.5\, E_X + 0.5\, E_{XC}^{LSDA} \tag{2.18}$$

The above formulation can be generalized as sum of the Hartree–Fock exchange energy and the exchange–correlation energy deriving from the approximations given in the previous sub–sections.

$$E_{XC} = aE_X^{HF} + (1-a)E_{XC}^{DFT} \tag{2.19}$$

Functionals of this sort, where a certain amount of exact exchange is incorporated are frequently called hybrid functionals, because they represent a hybrid between pure density functionals for exchange and exact Hartree–Fock exchange. The estimation of the constant a constant which governs the two contribution is empirical and many hybrid functionals were developed during the years optimized for different tasks, in particular:

- Becke first developed a 3–parameter functional expression exploiting two different generalized gradient approximation for the exchange and correlation energies, in particular the B and the PW91 functionals respectively. Moreover,

the exchange–correlation energy from the local density gradient approximation was exploited in order to produce the B3PW91 hybrid functional.

$$E_{XC}^{B3PW91} = aE_X^{HF} + (1-a)E_{XC}^{LSDA} + b\Delta E_X^B + E_C^{LSDA} + c\Delta E_C^{PW91} \quad (2.20)$$

- Stephens *et al.*[17] modified the B3PW91 hybrid functional by substituting the PW91 functional with the LYP correlation energy functional.

$$E_{XC}^{B3LYP} = aE_X^{HF} + (1-a)E_{XC}^{LSDA} + b\Delta E_X^B + (1-c)E_C^{LSDA} + c\Delta E_C^{LYP} \quad (2.21)$$

- Zhao *et al.*[18] proposed two different hybrid functionals in which the exchange and correlation energy functionals were approximated by the introduction of the second derivative of the electron density in the generalized gradient approximation turning it in what is called *meta*–generalized gradient approximation. The M06 an M06–2X hybrid functional developed differ essentially by the percentage of Hartree–Fock function which doubles passing from the first one to the second one.
- Chai *et al.*[19] developed a hybrid functional which exploits the Hartree–Fock uncorrelated exchange energy functional only the long–range electron–electron interactions. On the other hand, the short–range electron–electron interaction where computed trough the B97 functional as well as the correlation energy functional. The ωB97 hybrid functional was then improved by using a small fraction of the the Hartree–Fock uncorrelated exchange energy functional in order to compute short–range interaction giving rise to the ωB97X.

$$E_{XC}^{\omega B97} = E_X^{LR-HF} + E_X^{SR-B97} + E_C^{B97} \quad (2.22a)$$

$$E_{XC}^{\omega B97X} = E_X^{LR-HF} + c_x E_X^{SR-HF} + E_X^{SR-B97} + E_C^{B97} \quad (2.23b)$$

Subsequently[20], this last hybrid functional was improved by adding an empirical atomic–pairwise dispersion correction giving rise to the ωB97X–D.

2.3.3 Basis sets

The basis set is a set of mathematical functions from which it is possible to construct the wave function through the linear combination of the basis function and coefficients determined from the iterative solution. It sems reasonable to affirm that for a high–quality representation of the wave function, a very large basis sets are needed. Moreover, the basis functions must present complex nodal structures in order to provide a wave function which takes in account electron correlation. [10] These characteristics of the employed basis set alleges to very demanding computational procedures in highly correlated calculations.

From a physical point of view, the best basis set which could be chosen consists of Slater–type orbitals ϕ^{STO}. This such function are exponentials that mimic the exact eigenfunctions of the hydrogen atom exhibiting the correct cusp behaviour in proximity of the nuclei position. Moreover, these functions display a discontinuous derivative and the exponential form ensure the decay in the regions away from nuclei positions.[10] A typical expression for Slater–type orbitals can be written as follows:

$$\phi^{STO} = N\, r^{n-1}\, Y_{lm}\, e^{-\xi r} \tag{2.24}$$

Unfortunately, the resolution of two–electrons integrals is extremely difficult to compute with Slater–type orbital basis sets since no analytical techniques are available mainly due to the presence of cusps in these functions.[10] For this reason, in the wave function–based approaches to the resolution of the Schrödinger equation the set chosen consists on Gaussian–type orbitals ϕ^{GTO} rather than Slater–type orbitals.

$$\phi^{GTO} = N\, x^l\, y^m\, z^n\, e^{-\alpha r^2} \tag{2.25}$$

However, gaussian functions shows a maximum rather than a cusp which does not correctly represent the regions near to the nuclei whilst ensure an analytical resolution. Moreover, gaussian functions show a more rapid decay and an asymptotic trend rather than the more physical–rigorous behaviour of Slater functions. In order to overcome the abovementioned differences and resembles as much as possible a single Slater–type orbital function, Gaussian–

type orbitals are linearly combined to give rise to contracted Gaussian function ϕ^{CGF} in this case marked as primitives.[10]

$$\phi^{CGF} = \sum_{a=1}^{A} c_a \, \psi^{GTO} \tag{2.26}$$

The contracted Gaussian function has been exploited for different strategies in order to expand molecular orbital. The minimal sets are the simplest expansions which utilizes only one basis function for each atomic orbital. The STO–3G basis set, is a typical representation in which three Gaussian–type orbitals primitives are linear combined. Taking the carbon atom as an example, this basis set consists in one for 1s, 2s, $2p_x$, $2p_y$ and $2p_z$.

It seems clear that this expansion method is the quite inaccurate and it can give rise to qualitative interpretation of the system, as the set contains only one basis function for each atomic orbital and orbital shell. Since the minimal sets have the virtue of well describing the inner–core electrons, John Pople and coworkers[21] proposed a split–valance type basis set which exploit two contracted Gaussian function to describe the valence orbitals. The proposed example was the 4–31G basis set in which each atomic orbital is described by the linear combination of four Gaussian–type orbital and the valance orbitals were split in two parts consisting in three and one Gaussian functions. Subsequently, a lot of basis sets were born with the aim to further improve the People split–valance basis set. In particular, John People and coworkers[22] proposed and improved basis sets by *polarization functions*. The introduction of polarization functions ensures the distortion of the atomic orbitals in order to suit to the molecular environment. This is accountable to the greater number of angular nodal planes of polarization function than the occupied atomic orbitals. The most illustrious example is the 6–31G(d,p) basis sets. Following the last two results, it is clear that as more Gaussian–type orbitals are used in order to describe valence orbital, more accurate the basis set will be: typical example is the 6–311G(d,p) basis set. Later improvement to the basis sets were given by the introduction of gaussian function with very low exponent values, namely the diffuse functions. These functions allows the description of the region far away from the

nuclei as the exponent is low in value the functions are radial spread: typical examples is the 6–311+(d,p) basis set.

2.3.4 Solvation

Most of the *daily* chemistry is carried out in condensed phase, typically in solution.
In this scenario, any computational technique employed to understand processes which take place in solution needs to be armed with methods which allow a description of such environment. As with any other computational simulation, the methods aimed at describing solvation are more accurate the closer they get to the actual physics of the problem. However, this would imply an atomistic and fully quantum–mechanical description of both solvent and solute. In particular, taking into consideration the number of molecules needed to describe a solvation shell, it is clear that such a system is impossible to describe with current resources at a quantum chemical level. A good compromise between approximation and computational affordability is achieved by modelling the solvent as if it only had bulk properties.

2.3.4.1 Continuum methods

Continuum methods simulate the effect of the solvent by embedding the system in a continuum medium described using macroscopic properties. These methods have the advantage of being computational cheap and to take into account long–range effects of the solvation process. However, the low cost in term of computational resources is to relate to the loss of specific solute–solvent interactions which arise from the discrete molecular nature of the solvent.[3]
The key magnitude when using these methods is the work needed to transfer one molecule of solute from the vacuum to the solution: this magnitude corresponds to the Gibbs free energy of solvation.

This free energy can be divided in three main contributes which are accountable to the electrostatic interaction between solute and solvent, to the reorganization of the solvent molecules around the solute and both local attractive and repulsive solute–solvent short–range interactions.[3]

$$\Delta G_{solv} = \Delta G_{el} + \Delta G_{cav} + \Delta G_{SRIs} \tag{2.27}$$

The term responsible for the reorganization of the solvent molecule in presence of the solute is namely the cavitation energy. This term is usually represented by the cavitation free energy of a sphere in a solvent composed of spheres of radius at a given temperature, pressure and density. The calculation of the attractive and repulsive solute–solvent interactions is much more complicated, since it is a purely quantum mechanical effect that is hard to model when there are no explicit solvent molecules. The main problems with these two free energies are related to their quite large and of opposite signs values and the absence of experimental values to compare with them. As a result, they are often evaluated together using an empirical function based on empirically determined surface tension or atomic solvation parameters. Since these two free energies are calculated, the solvation it is only about the evaluation of the electrostatic interactions. As stated before, the solute is located in a cavity of the solvent which charges interact with the electron density of the first one.[3] Many different ways of treating solvation were proposed during the years, in particular:

- Solvent considered as dielectric continuum in which the solution for the electrostatic free energy term passes through the resolution of the Poisson equation.
- Polarizable continuum method in which the solvent is represented using an apparent surface charge density spread on the cavity surface.
- Conductor–like screening model in which the molecule is considered surrounded by a surface that represents the frontier between the solute electron density and the solvent. This boundary surface is assumed to be a perfect conductor not a dielectric surface.

2.4 References

1. Cao, Y. *et al.* Quantum Chemistry in the Age of Quantum Computing. *Chem. Rev.* 119, 10856–10915 (2019).

2. Foresman, J. B. & Frisch, Æ. *Exploring chemistry with electronic structure methods. Gaussian Inc, Pittsburgh, PA* (2015).

3. Tantillo, D. J. *Applied theoretical organic chemistry. Applied Theoretical Organic Chemistry* (2018).

4. Rivalta, I. Lecture Notes 2020.

5. Saunders, M. *et al.* Conformations of Cycloheptadecane. A Comparison of Methods for Conformational Searching. *J. Am. Chem. Soc.* 112, 1419–1427 (1990).

6. Engler, E. M., Andose, J. D. & von Schleyer, P. R. Critical Evaluation of Molecular Mechanics. *J. Am. Chem. Soc.* 95, 8005–8025 (1973).

7. Allinger, N. L., Yhu, Y. H. & Lii, J.–H. Molecular Mechanics. The MM3 Force Field for Hydrocarbons. *J. Am. Chem. Soc.* 111, 8552–8566 (1989).

8. Harder, E. *et al.* OPLS3: A Force Field Providing Broad Coverage of Drug–like Small Molecules and Proteins. *J. Chem. Theory Comput.* 12, 281–296 (2016).

9. Adams, J. B. Bonding Energy Models. in *Encyclopedia of Materials: Science and Technology* 763–767 (2001). doi:10.1016/b0–08–043152–6/00146–7.

10. Koch, W. & Holthausen, M. C. *A Chemist's Guide to Density Functional Theory.* (2001). doi:10.1021/ja004799q.

11. Szabo, A. & Ostlung, N. S. *Modern Quantum Chemistry.* (1996). doi:10.1119/1.1973756.

12. Hohenberg, P. & Kohn, W. Inhomogeneous Electron Gas. *Phys. Rev.* 136, B864–B871 (1964).

13. Kohn, W. & Sham, L. J. Self–Consistent Equations Including Exchange and Correlation Effects. *Phys. Rev.* 140, A1133–A1138 (1965).

14. Becke, A. D. Density–fnnctional exchange–energy approximation with correct asymptotic behavior. *Phys. Rev.* 38, 3098–3100 (1988).

15. Cramer, C. J. *Essentials of Computational Chemistry.* vol. 43 (2004).

16. Becke, A. D. A new mixing of Hartree–Fock and local density–functional theories. *J. Chem. Phys.* 98, 1372–1377 (1993).

17. Stephens, P. J., Devlin, F. J., Chabalowski, C. F. & Frisch, M. J. Ab Initio calculation of vibrational absorption and circular dichroism spectra using density functional force fields. *J. Phys. Chem.* 98, 11623–11627 (1994).

18. Zhao, Y. & Truhlar, D. G. The M06 suite of density functionals for main group thermochemistry, thermochemical kinetics, noncovalent interactions, excited states, and transition elements: Two new functionals and systematic testing of four M06–class functionals and 12 other function. *Theor. Chem. Acc.* 120, 215–241 (2008).

19. Chai, J. Da & Head–Gordon, M. Systematic optimization of long–range corrected hybrid density functionals. *J. Chem. Phys.* 128, (2008).

20. Chai, J. Da & Head–Gordon, M. Long–range corrected hybrid density functionals with damped atom–atom dispersion corrections. *Phys. Chem. Chem. Phys.* 10, 6615–6620 (2008).

21. Ditchfield, R., Hehre, W. J. & Pople, J. A. Self–consistent molecular–orbital methods. IX. An extended gaussian–type basis for molecular–orbital studies of organic molecules. *J. Chem. Phys.* 54, 720–723 (1971).

22. Frisch, M. J., Pople, J. A. & Binkley, J. S. Self–consistent molecular orbital methods 25. Supplementary functions for Gaussian basis sets. *J. Chem. Phys.* 80, 3265–3269 (1984).

3. Aim of the work

The aim of the present work is to exploit many of the computational chemistry techniques illustrated in the previous chapter to derive the transition state geometries of an asymmetric primary–amine catalysed Michael addition reaction in presence of different organic acid cocatalysts. All the study is focused on the addiction of the enamine resulting from the reaction between cyclohexanone and 9–*epi*–9–amino–9–deoxy–quinine to *trans*–β–nitrostyrene.

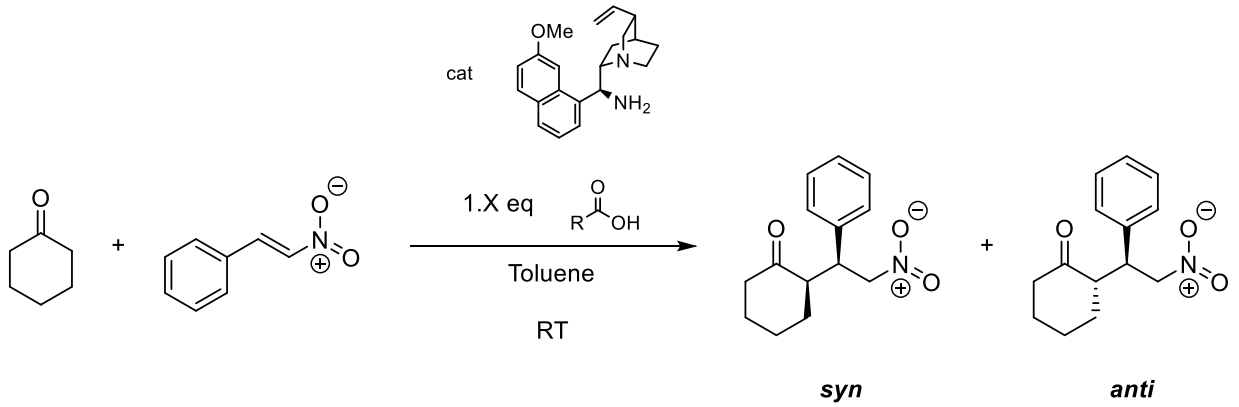

Figure 3.1. Asymmetric primary amine–catalysed Michael addition reaction between cyclohexanone and *trans*–β–nitrostyrene via enamine.

In this scenario, the information on energetically favoured transition states geometries is useful to show the difference in activity of the same reaction partner in presence of different cocatalysts. Moreover, it is possible evaluate how the different functionalities on the organic acids may affect the diasteromeric ratio between the reaction products.

Finally, the results obtained in this work are used to corroborate the research conducted by professor Alessia Ciogli and professor Claudio Villani's group from "Università di Roma, Sapienza" on such reacting system. In particular, the group focused its attention on finding the optimal reaction condition in terms of molar ratio of reagents, nature of the solvent and type of organic acid cocatalysts through mass spectrometry with different interfaces.

3.1 Michael addition

Since its first publication in 1887 by Arthur Michael,[1] Michael addition reaction represents one of the most powerful synthetic pathways for the formation of carbon–carbon bonds. The reaction is conducted in the presence of electrophilic substrate which present a carbon–carbon double bond in conjugated to an electron withdrawing group and a nucleophilic species, typically enolates.[2]

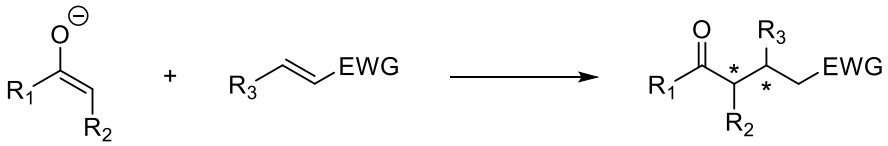

Figure. 3.2. Michael addition reaction generic pathway.

The electrophilic reaction partner is typically an α,β–unsaturated carbonyl compound, however, vinylic and alkynic substrate functionalized with different electron–withdrawing substituents which activate carbon–carbon unsaturated bond to nucleophilic attack such as nitro, cyano, or sulfonyl fragment can be exploited.[2] Moreover, as a matter of fact, the reaction pathway (figure 3.1) which will be discussed in the following chapter involves *trans*–β–nitrostyrene as the electrophilic substrate. Moreover, enamines are extensively exploited in Michael addition reaction since they are stronger nucleophilic analogue to the enols, as described in the first chapter. In this scenario, the cyclohexanone has been chosen as carbonylic substrate involved in the formation of the enamine.

3.2 Quinine primary amine derivative as catalysts

The reaction pathway on which all the experimental work has been conducted exploited a cinchona alkaloid –primary amine derived as the organic catalyst. As stated in the first chapter, asymmetric aminocatalysed reaction pathways are today one of the most useful strategies to obtain chiral products with high enantiomeric excess values with small organic molecules. Even if proline mediated reactions have been central in the field of asymmetric organocatalysis, in the past ten years, chiral primary amines have arisen as powerful catalysts too. In particular, primary amines derived from cinchona alkaloids have been recognized as a reliable and general catalyst class with a high synthetic potential for aminocatalysis.[3] The cinchona–alkaloids show a quinuclidinic bicyle fragment which ensure a Lewis basic site in the molecular skeleton. The presence of such functionality allows primary amine to be succefully employed in the stereoselective functionalisation of a huge variety of sterically hindered carbonyl compounds, which functionalisation trough secondary amines or even metal–centre catalysis result quite challenging.

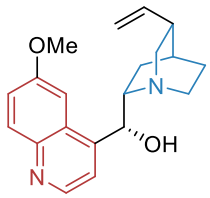

Figure 3.3. Representation of quinine structure: in red, the quinolinic moiety; in blue, the quinuclidinic bicycle responsible for the Lewis basicity.

Cinchona alkaloid–primary amine derivative catalysts can be easily prepared from readily available and inexpensive natural sources which offer both diasteroisomers. Beside of their stereochemical relations, this diastereoisomeric pair generally acts as *quasi*–enantiomeric catalysts. Following the IUPAC definition, *quasi*–enantiomers are closely related but constitutionally different compounds, which behave as enantiomers in the case of chiral induction reactions. The use of such pair of diasteromeric species allows access to both enantiomers of a product in a broad range of asymmetric reactions.[4] However, it has been

observed that while one of the members of the pair allows efficient enantioselective conversion, the corresponding *quasi*–enantiomer does not yield similar results. Even if the origin of this discrepancy is not clear, the different in catalytic activity is to account to the small structural differences between the species.[4]

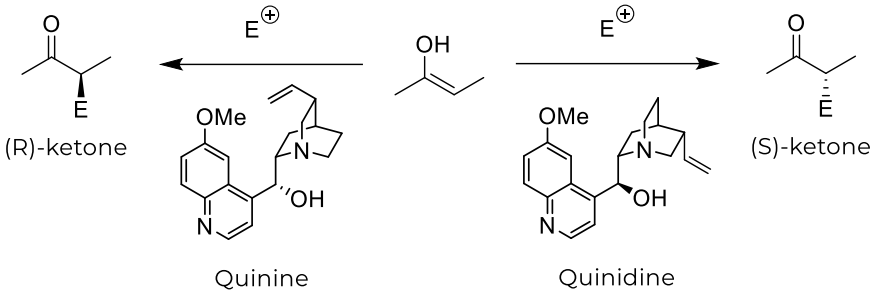

Figure 3.4. Reactions of prochiral enol with an electrophile catalysed by two different *quasi*–enantiomeric alkaloids leading to different enantiomers.

The deoxy–*epi*–amination of the alcoholic moiety in the cinchona alkaloids is an operationally simple and relatively fast procedure which is performed by first introducing an azide via the Mitsunobu reaction. This reaction pathway allows the inversion of the configuration of secondary alcohol compounds with high stereoselectivity. The Mitsunobu protocol involves the reaction of the abovementioned species and a nucleophile in the presence of triphenylphosphine and diisopropyl azodicarboxylate. The azide source is usually the diphenyl phosphoryl azide.[3]

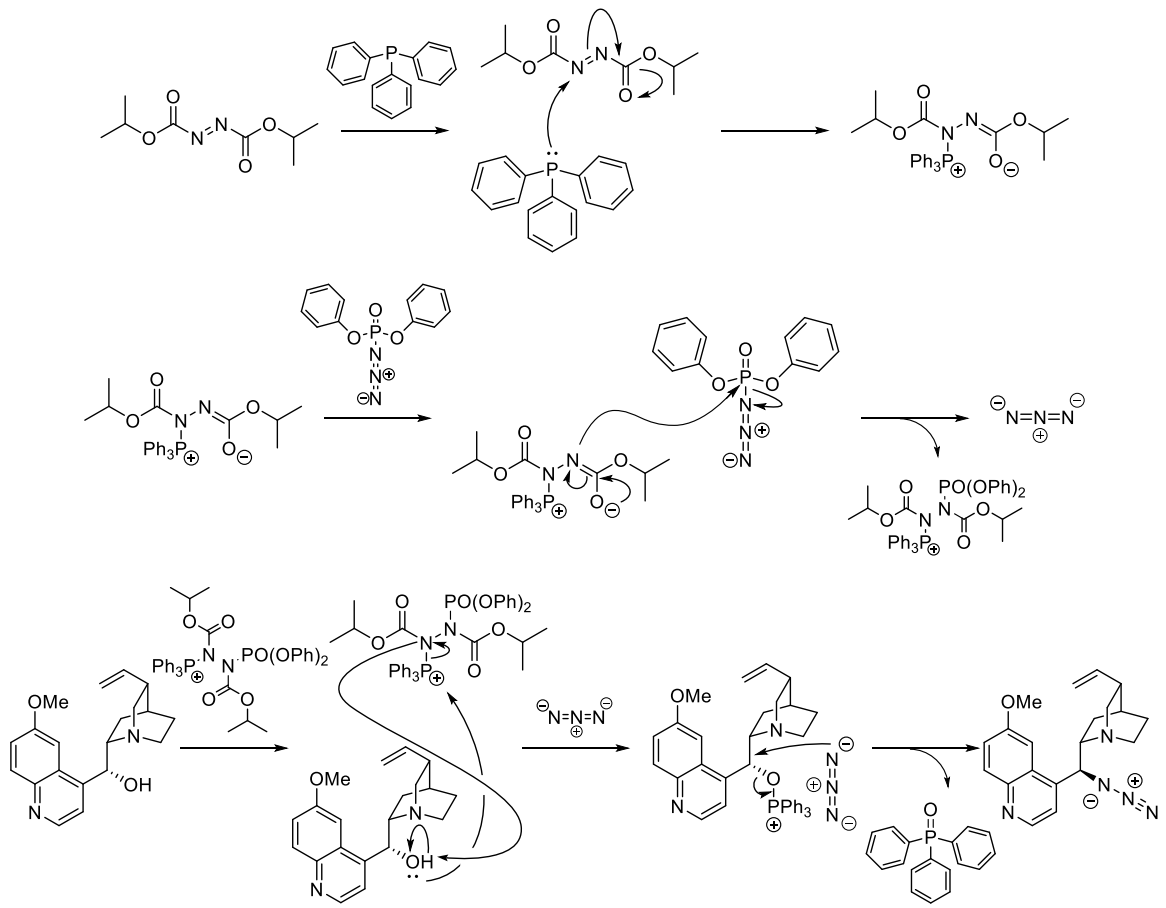

Figure 3.5. Mitsunobu's reaction mechanism for the conversion of quinine into its corresponding azide–derivative.

The reduction of the obtained azide–functionalized intermediate is performed in the same pot. The intermediate reacts with an excess of triphenylphosphine according to the Staudinger reaction to form an aminophosphorane that is subsequently hydrolysed into an amine moiety.[3]

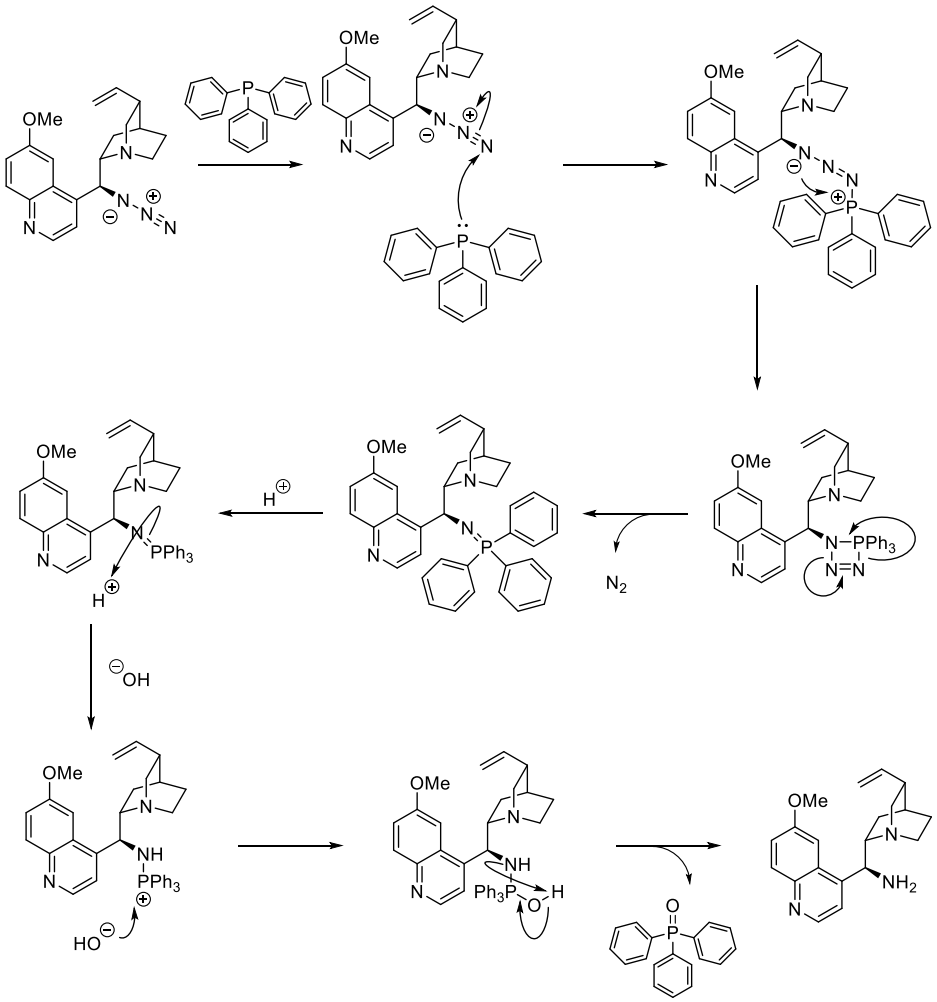

Figure 3.6 Staudinger's reaction mechanism for the conversion of quinine azide–derivative into 9–*epi*–9–amino–9–deoxyquinine.

3.3 Acid cocatalysts

The rection has been experimentally conducted one–pot with an organic acid compound in little excess with respect to the catalyst. As stated in the first chapter, the use of Brønsted acids facilitate the formation of the enamine due to the fact that it promotes the dehydration of the hemiaminal. Moreover, it has been demonstrated[5] that in some cases the presence of such species can also slightly improve the catalytic efficiency of the reaction in term of diasteroselectivity. For this reason, professor Ciogli and professor Villani's group used different organic aromatic acids in order to quantitatively evaluate this effect on the reaction

of interest. In particular, 4–nitrobenzoic acid and 4–hydroxybenzoic acid have attracted high interest.

3.4 References

1. Michael, A. & Schulthess, O. Ueber die Addition von Natriumacetessig– und Natriummalonsäureäthern zu den Aethern ungesättigter Säuren. *J. für Prakt. Chemie* 45, 55–63 (1892).

2. Carey, F. A. & Sundberg, R. J. *Advanced Organic Chemistry Fifth Edition, Part B: Reactions and Synthesis*. (2008). doi:10.1093/jaoac/34.2.496.

3. Cassani, C., Martín–Rapún, R., Arceo, E., Bravo, F. & Melchiorre, P. Synthesis of 9–amino(9–deoxy)epi cinchona alkaloids, general chiral organocatalysts for the stereoselective functionalization of carbonyl compounds. *Nat. Protoc.* 8, 325–344 (2013).

4. Ričko, S., Izzo, J. A. & Jørgensen, K. A. Insights on the Pseudo–Enantiomeric Properties of Bifunctional Cinchona Alkaloid Squaramide–Derived Organocatalyst. *Chem. – A Eur. J.* 26, 15727–15732 (2020).

5. Mukherjee, S., Yang, J. W., Hoffmann, S. & List, B. Asymmetric enamine catalysis. *Chem. Rev.* 107, 5471–5569 (2007).

4. Results and discussion

To reach the objectives outlined in the previous chapter, a computational strategy has been developed for all the substrates analysed. The adopted route can be briefly summarised as follows:

1. Conformational analysis for the evaluation of the low energy conformation population for each chemical species involved in the transition state.
2. DFT geometrical optimization to find a minimum for the conformers belonging to each reagent.
3. Combination of optimized cyclohexanone and quinine amino–derivative conformers and further optimization to a minimum. The set of lowest energy conformations are obtained for the reacting enamine.
4. Again optimization with the addition of the previously minimized organic acid conformers to derive the enamine–acid complex conformers.
5. Approaching relaxed scan between the enamine salt conformers carbon atom in α–position and the *trans*–β–nitrostyrene conformers carbon atom in β–position to the nitro group. This will yield transition state initial geometry guesses that will be refined in the next step.
6. A final optimization to a transition state of the structure resulting from a previous approaching relaxed scan between the involved reaction centres through the Berny algorithm. Boltzmann population is also calculated to derive the diasteromeric ratio resulting for comparison with the experimentally obtained values.

In the following five section, the abovementioned steps will be applied and explained for the determination of the diasteromeric ratio for the reaction co–catalysed by 4–nitrobenzoic acid.

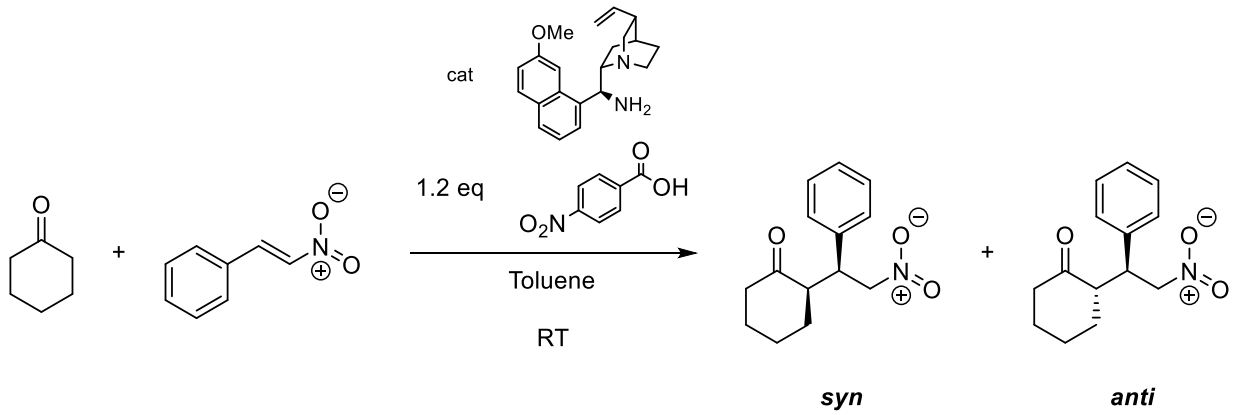

Figure 4.1. Michael addition of cyclohexanone to *trans*–β–nitrostyrene catalysed by 9–*epi*–9–amino–9–deoxyquinine and 4–nitro–benzoic acid.

4.1 Conformational analysis

The conformational space analysis has been carried out with the *MacroModel 12* software developed by *Schrödinger LLC*. The parameters for conformer analysis exploited for all species have been chosen according to the protocol proposed by Willoughby and coworkers.[1] In particular, the Monte Carlo multiple minimum method has been chosen for the random sampling of the possible conformation while the OPLS3e force–field has been exploited in the minimization process as force–field. Following the criteria set by Willoughby, the number of steps has been set to 5000. The conformers number found for each reagent are shown in table 4.1.

Table 4.1. Number of conformers found for each reagent.

Reagent	Number of Conformers found
cyclohexanone	3
trans–β–nitrostyrene	1
4–nitrobenzoic acid	1
9–*epi*–9–amino–9–deoxyquinine	41

The three cyclohexanone conformer structures obtained are shown in figure 4.2. The first conformer **A** shows a chair–like structure while both conformers **B** and **C** show twisted–boat structure with good approximation.

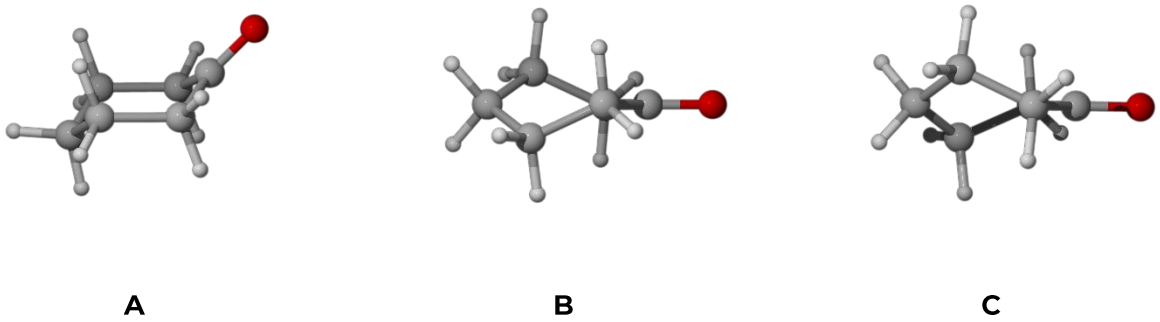

Figure 4.2. Three ground state cyclohexanone conformers found.

Following the work of Allinger *et al.*[2], it is possible to state that structure A represent the lowest energy conformation between all the accessible ones for cyclohexanone. However, the other two conformers are good representation of local minimum corresponding to a twisted–boat structure.

Finding only one conformer for both *trans*–β–nitrostyrene and 4–nitrobenzoic acid is not a surprising result. The all–sp^2–hybridized atoms characteristic of the structures have, in fact, prevented dihedral rotation which are the core of the Monte Carlo multiple minimum algorithm.

The number of 9–*epi*–9–amino–9–deoxyquinine conformers is quite high since the molecule is constituted by 49 atoms and many rotatable dihedrals, as expected.

4.2 DFT optimization of reagent conformers

Since the focus of the first part of the computational strategy is the screening of the lowest minimum energy conformers for each single reagent involved, all the retrieved conformers have been further optimized to an energy minimum with a density functional calculation.

The DFT calculations presented in this work have been carried out using *Gaussian 16*[3] developed by *Gaussian Incorporated*. First of all, following a consolidate protocol[4], two consecutive optimizations have been performed of all the conformers using the B3LYP hybrid functional the 3–21G basis set for the first optimization round and the 6–31G(d) for the second optimization. Redundant conformer geometries were discarded between the first and the second optimization rounds.
The number of DFT optimized conformers resulting from the second step are reported in table 4.2.

Table 4.2. Number of different conformers for each reagent lasting after B3LYP/6–31 G(d) optimization.

Reagent	Number of different optimized conformers
cyclohexanone	2
trans–β–nitrostyrene	1
4–nitrobenzoic acid	1
9–*epi*–9–amino–9–deoxyquinine	27

For what concerns cyclohexanone, the set of conformers reduced its elements from three to two after the minimization route. The two conformers relative electronic energies differ by 3.73 kcal·mol^{-1} and their structure are reported in figure 4.3.

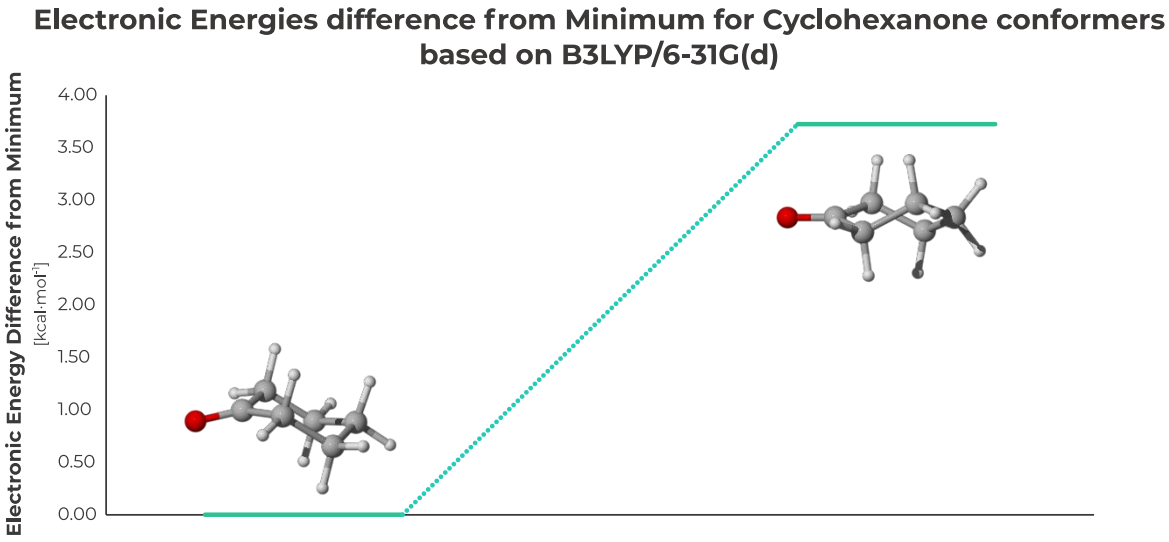

Figure 4.3. Electronic energy difference from global minimum for cyclohexanone conformers.

As foretold in the previous section, the lowest energy conformer shows a chair–like structure while the other one shows a twisted–boat structure. However, the difference in electronic energy between the two conformers is greater with comparison to the one reported by Allinger and coworkers (which is less than 3 kcal·mol^{-1})[2]. Even if this result is not consistent with the previous results, the difference of almost 4 kcal·mol^{-1} between the two conformation allows discarding the twisted–boat conformers for the further calculations.

For what concern both *trans*–β–nitrostyrene and 4–nitrobenzoic acid, the two optimizations to energy minimum do not afford any modification in the number of conformers. However, this step allows for a further optimization of the geometrical parameters of the two molecules.

The 9–*epi*–9–amino–9–deoxyquinine conformers have greatly reduced their number after these DFT calculations. In this scenario, the Boltzmann distrution has been calculated trough the Boltzmann equation. The Boltzamann distribution is extremely useful since it ensures a better understanding of which conformers have an higher statistical weight in the ground state population. The percentege of the i^{th} conformer is calculated by weighting its energy over the sum of the energy of the all n conformers present as follows:

$$\%_i = \frac{e^{\frac{E_i}{RT}}}{\sum_n e^{\frac{E_n}{RT}}} \tag{4.1}$$

The Boltzmann population distribution for the 9–*epi*–9–amino–9–deoxyquinine conformers are reported in figure 4.4 where the *Qd* acronym stands for quinine–derivative and the following integer number represent the order in which these conformers have been optimized.

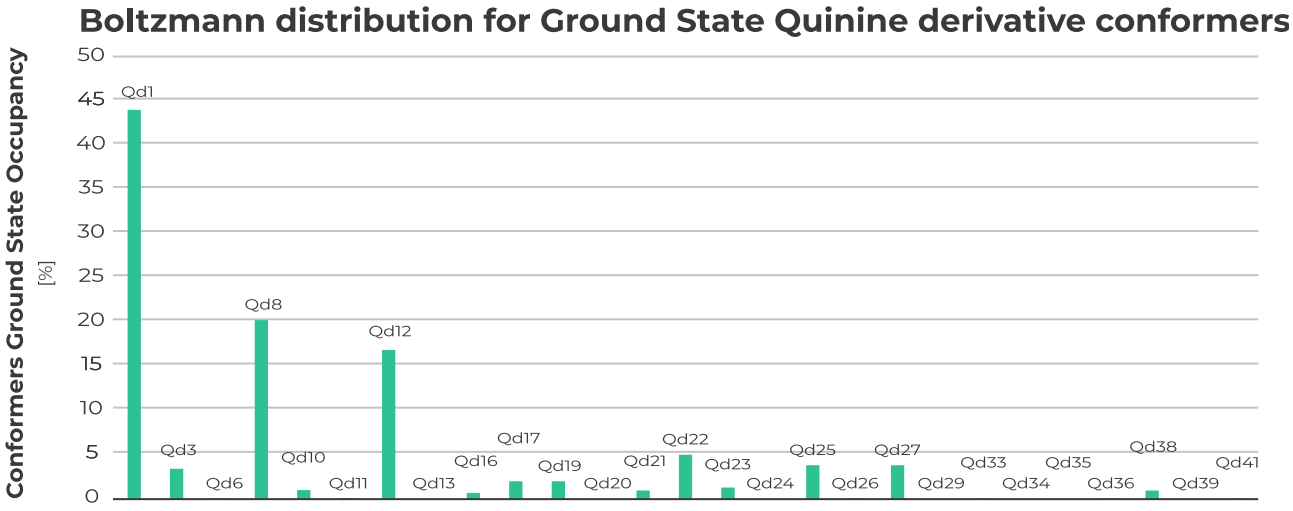

Figure 4.4. Boltzmann distribution of quinine amine–derivative conformers.

From the above plot, it is possible to conclude that more than the 85% of the ground state population is constituted by the derivatives 1, 8, 12 and 22. It is well established that cinchona alkaloids[5] and their derivatives can adopt four energetically preferred conformations, two open and two closed forms which differ for the relative orientation of the quinoline moiety and the quinuclidinic cage. Vayner *et al.*[5] showed that these different relative orientations are originated by rotation around two carbon–carbon bonds, in particular the bond between chiral carbon and quinuclidine B_1 and the bond between chiral carbon and quinoline moiety B_2.[5,6]

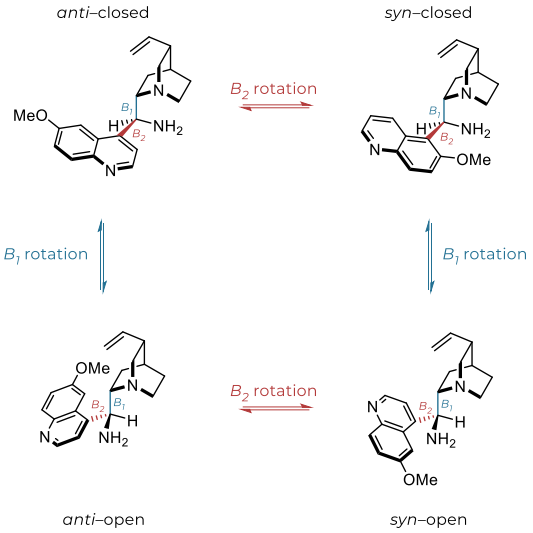

Figure 4.5. Four energetically favoured quinine amine–derivative conformers.

Moreover, it has been demonstrated in Moran' work[6] that the *anti*–open conformation is the one which populates the majority of the ground state population. It is possible to see from its structure (figure 4.6) that in our conformational search the conformer labeled with the acronym *Qd1* shows exactly the *anti*–open conformation and as a matter of fact, it is the one with the highest statistical weight in the computed Boltzmann population distribution.

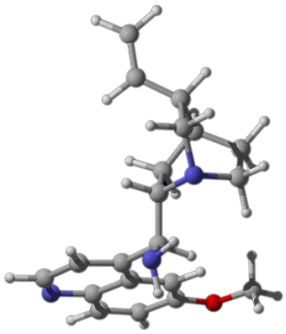

Figure 4.6. *Ball and stick* representation of *Qd1* structure which correspond to the *anti*–open conformation.

It is also known that the *syn*–open is the second most populated conformation in the ground state. It is possible to see from their structure visible in figures 4.7(A) and 4.7(B) that the conformers *Qd8* and *Qd12* are both *syn*–open conformations which differ one another by the relative orientation of the methyl fragment which belong to the methoxy–quinolinic moiety

with respect to the quinuclidinic cage. To distinguish the two conformers and highlight the abovementioned relative disposition it has been chosen the caption '*syn*–Me' and '*anti*–Me'.

Figure 4.7. A: *Ball and stick* representation of *Qd12* structure which correspond to the *syn*–Me–*syn*–open conformation; B: *Ball and stick* representation of *Qd22* structure which correspond to the *anti*–Me–*syn*–open conformation.

However, it is possible to notice from figure 4.4 that the second most populated conformation in the ground state corresponds to conformer *Qd8*. By looking at its structure (figure 4.8), it is possible to notice that it presents a half–way rotation of the τ_2 torsional angle alleging to a structure which can be rationalized as a mean point between conformer *Qd1* and *Qd12*. For this reason, it has been assigned the caption *HW1–12* which stand for half–way between the *anti*–open and the *syn*–Me–*syn*–open conformers.

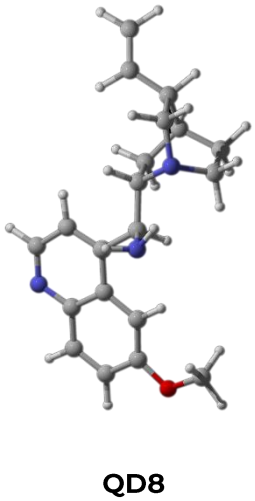

Figure 4.8. *Ball and stick* representation of *Qd8* structure which correspond to the *HW1–12* conformation.

Up to this point, the comparison between the experimental results obtained and previous studies are in good agreement.

Lastly, it has been decided to involve in the following steps not only the four conformers described above but also other quinine–derivative conformers, which were firstly excluded in the previous evaluation. Boltzmann distribution granted a decreasing order in terms of statistical weight. Following this order, as many conformers were added as necessary to ensure the evaluation of 95% of the ground state population. In this way the set has been considered complete. The electronic energy distribution of the 9 elements of the set is reported in figure 4.9.

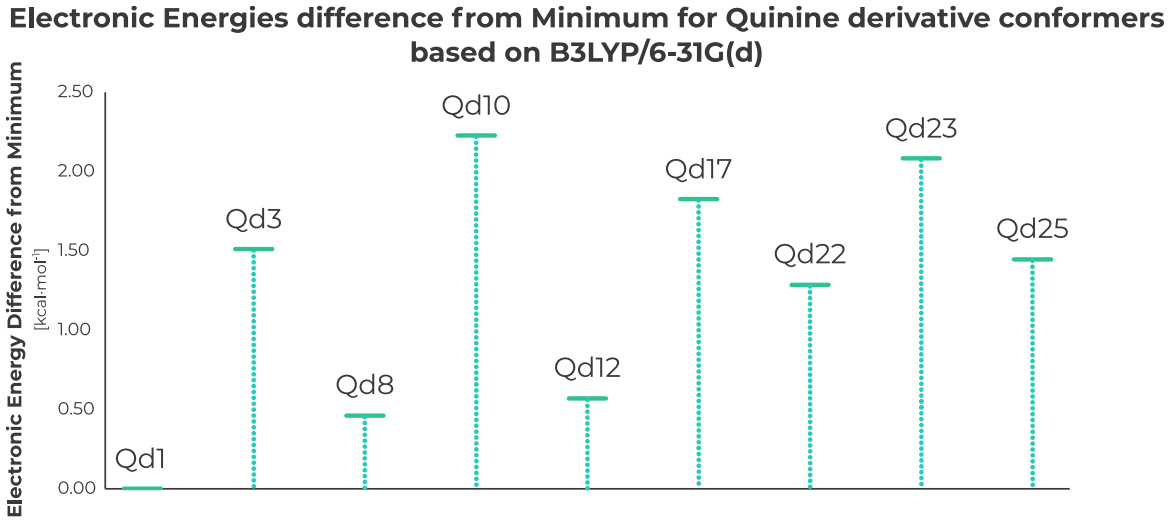

Fig 4.9. Electronic energy difference relative to the global minimum for quinine amine–derivative *Qd* conformers.

The chosen set is characterised by a difference in terms of electronic energy between the global minimum conformer and the other eight not exciding 2.23 kcal·mol^{-1}.

4.3 DFT optimization of enamine conformers

Starting from the nine quinine–derivative conformers and the chair–like cyclohexanone structure, the set of enamine conformers have been constructed using *GaussView 6*[7]

developed by *Gaussian Inc.* The cyclohexanone carbonyl group has been removed as well as one hydrogen bonded with the nitrogen atom of the quinine amine–derivative. Therefore, a new nitrogen–carbon bond has been built. Subsequently, another hydrogen atom has been removed from one carbon atom in the six–member ring in α–position to the carbon–nitrogen bond. This allows for the construction of a double carbon–carbon bond.

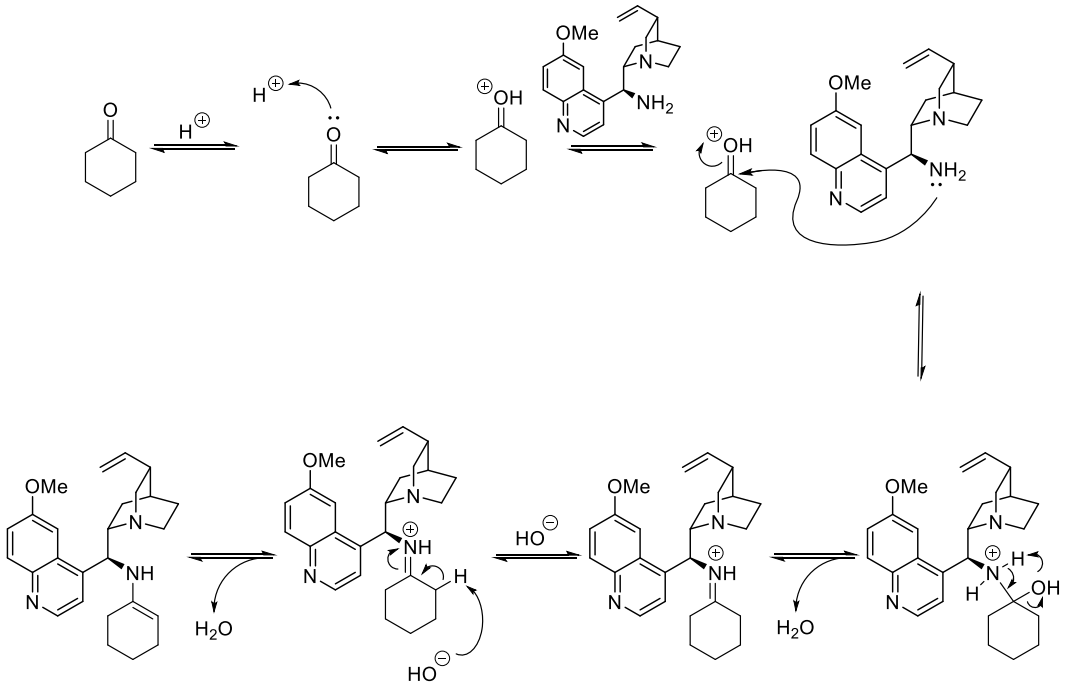

Figure 4.10. Enamine formation mechanism for the reaction between cyclohexanone and 9–*epi*–9–amino–9–deoxyquinine.

The *crude* conformer structures have been optimized to a minimum trough a DFT calculation which used B3LYP as hybrid functional and the 6–31G(d) basis set. This calculation has been applied to all the nine conformers highlighted in the Boltzmann distribution and it is composed by only two conformers. The result is reported in figure 4.11, where the *E* acronym stands for enamine and the two following integer numbers represent both the cyclohexanone and quinine–derivative conformer number.

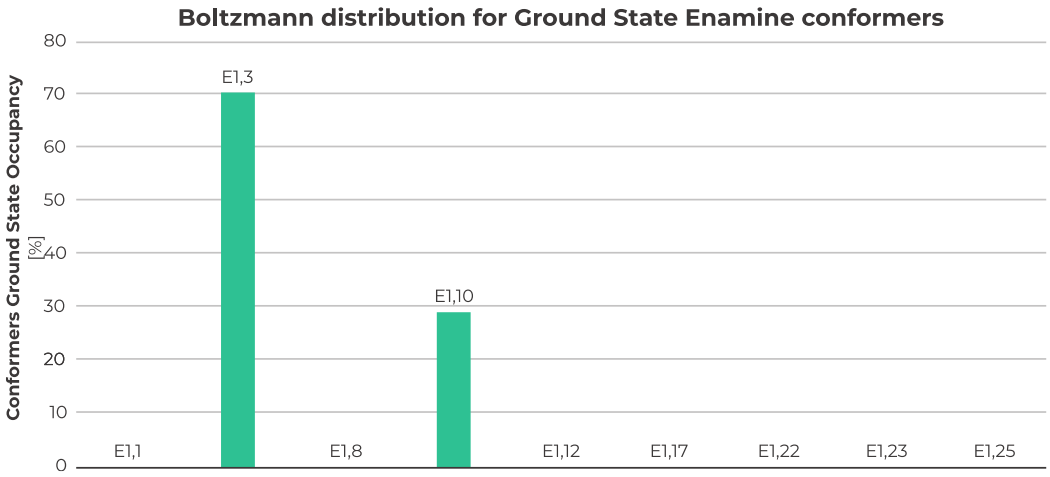

Figure 4.11. Boltzmann distribution of enamine conformers.

The structures relative to the lowest energy enamine conformers obtained are reported in figure 4.12 and they are derived from both an *anti*–open and a *syn*–open quinine–derivative conformers, as it was predictable. However, it is possible to notice both from their caption and structure that the quinine amine–derivative fragments are not totally matching the *anti*–open and *syn*–open conformation highlighted in the previous section. In fact, these last ones show different dihedral angles of the vinyl fragment with the quinuclidinic cage when compared to the corresponding *Qd1* and *Qd12* conformers.

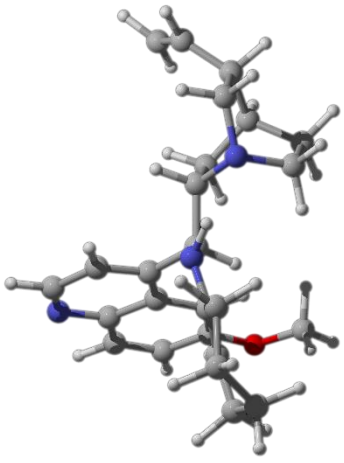

anti–closed enamine conformer

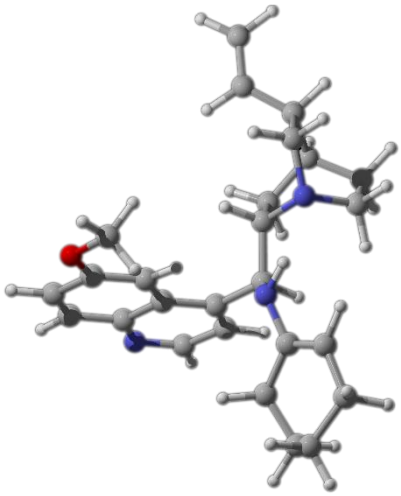

syn–Me–*syn*–closed enamine conformer

E1,3 (A) **E1,10 (B)**

Figure 4.12. A: *Ball and stick* representation of *E1,3* structure which correspond to the *anti*–open conformation; B: *Ball and stick* representation of *E1,10* structure which correspond to the *syn*–Me–*syn*–open conformation.

The difference in terms of electronic energy between *E1,3* and *E1,10* has been calculated to be less than 1 kcal·mol^{-1} as reported in figure 4.13.

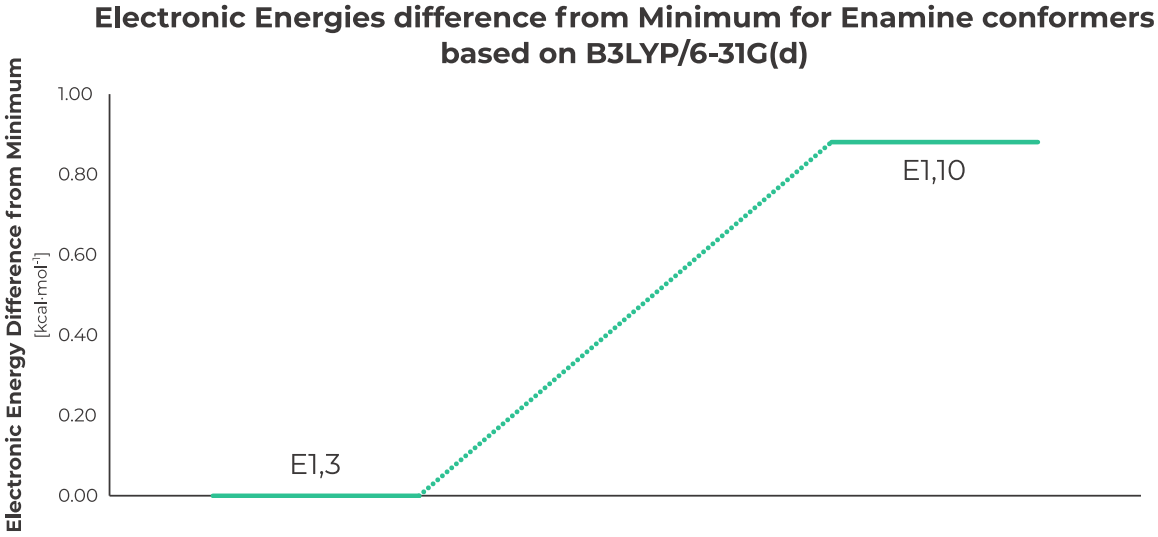

Figure 4.13. Electronic energy difference from global minimum for enamine *E* conformers.

4.4 DFT optimization of enamine salts conformers

Since the enamine conformer set has been built and optimized to a minimum, the following step in the computational route consisted in the introduction of the organic acid in the system. The preparation of the enamine–acid complex conformers is a crucial step since the aim of the work is actually to find an explanation of the different catalytic efficiency in the presence of different acidic substrates.

4.4.1 Insights for the structure building

The experimental results obtained by professor Ciogli' and professor Villani' group highlighted that the addition of an acidic cocatalyst enhances the catalytic performances in terms of diasteromeric ratio. Since the reaction is one–pot, the acid can virtually react with both cyclohexanone and the quinuclidine nitrogen atom. However, even if the acid catalysis moves the equilibria towards the enamine formation, the quinuclidine is a sufficiently strong base to make the protonation of the nitrogen atom favourite over the protonation of the oxygen atom which belongs to the cyclohexanone. From these, it has been suggested that the acid firstly protonate the nitrogen atom of the quinuclidinic moiety and then its counter–ion sits in the space pocket around it trying to adopt a disposition with the minimum impact on the energy of the system. In this scenario, the enamine–organic acid complex conformers have been constructed in the same way as the enamine conformers. The hydrogen atom has been moved from the carboxylic moiety to the nitrogen atom using *GaussView 6*. The system has been optimised to a minimum by a DFT calculation; therefore, the hybrid functional has been carefully chosen.

4.4.2 Comparison of DFT methods

Since the construction of enamine–acid complex conformers is the key step to obtain the aforementioned goal, it has been decided to benchmark four different DFT methods. In particular, the previously B3LYP/6–31G(d) optimized enamine conformers have been newly

minimized with other three different hybrid functionals to find out which one has the best performance when coupled with 6–31G(d) basis set. This information has been practically achieved by comparing the Boltzmann distribution obtained by exploiting each hybrid functional with the one obtained by optimizing the same system with a much more expensive B3LYP/6–311+G(d,p) based DFT calculation. At the end of this benchmarking process the best–performing hybrid functional will be used in the minimization of the enamine salt conformers. The three hybrid functionals of choice were B3LYP–D3, M06–2X and ωB97X–D. The choice of B3LYP/6–311+G(d,p) as the yardstick is due to two main factors:

- The completeness of the basis set granted by the triple splitting of the GTO in order to describe the valance orbitals, the presence of both p and d polarization functions and the use of a diffuse function.
- The robustness that this hybrid functional has demonstrated in the description of such systems. In fact, it is common practise to employ this functional.

The Boltzmann population distribution calculated with the B3LYP hybrid functional and the basis set described above is reported in figure 4.14 and compared to the one calculated in section 4.3.

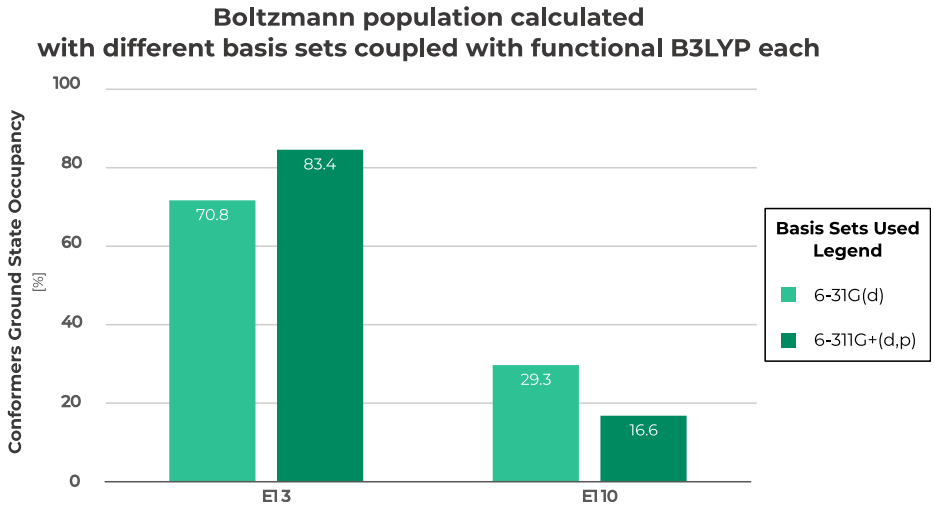

Figure 4.14. Comparison of Boltzmann distribution of quinine enamine conformers calculated with different basis sets.

In figure 4.15 are reported, instead, all the Boltzmann distribution calculated with the four hybrid functionals with the 6–31 G(d) basis set.

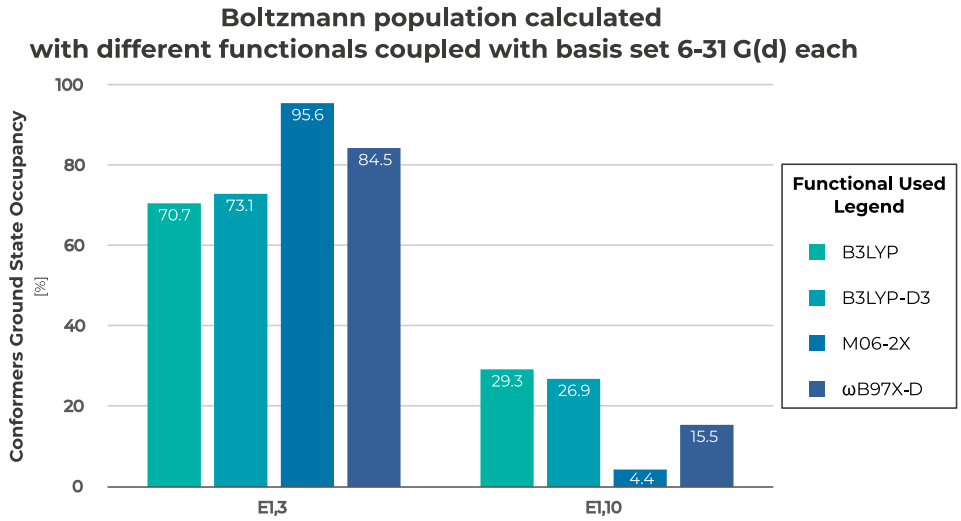

Figure 4.15. Comparison of Boltzmann distribution of quinine enamine conformers calculated with different hybrid functionals.

The most interesting result it is the one obtained with the couple ωB97X–D/6–31G(d). The Boltzmann distribution obtained with this hybrid functional is one–percent less than the one obtained with the much more computationally expensive B3LYP/6–311+G(d,p) used as a benchmark. Even if the two hybrid functional/basis set couples have led almost to the same results concerning conformers distribution in the ground state, they showed a big difference in the wall–time neede to compl,ete the calculations with the same memory and shared processors. In particular, the B3LYP/6–311+G(d,p) optimization took about 5 hours to complete while the ωB97X–D/6–31G(d) took less than two hours. From these results, it has we chose the ωB97X–D hybrid functional as the best–performing in the optimization of such system over the other three functionals and it has been used for all the further calculations.

4.4.3 DFT calculations

Since the hybrid functional has been chosen and the *crude* conformer structure has been constructed following the above two subsections, another DFT optimization to a minimum has been carried out. However, further optimizations have been carried out only on the minimized complex conformers in which the rotation in space of the acid counter–ion have been slightly changed. The different counter–ion rotations have been performed nearby the diaminic "arc" identified by the dihedral ranging from the enamine nitrogen atom to the hydrogen atom which belongs to the protonated quinuclidine. This process has been done to highlight if have been existed a counter–ion spatial–rotation which further minimize the electronic energy of the previously optimized complex conformers. The outcome of all the optimizations is reported in figure 4.16 where the conformers are represented by the *ES* acronym stands for enamine salt and the two following integer which represent the enamine conformer exploited for the structure.

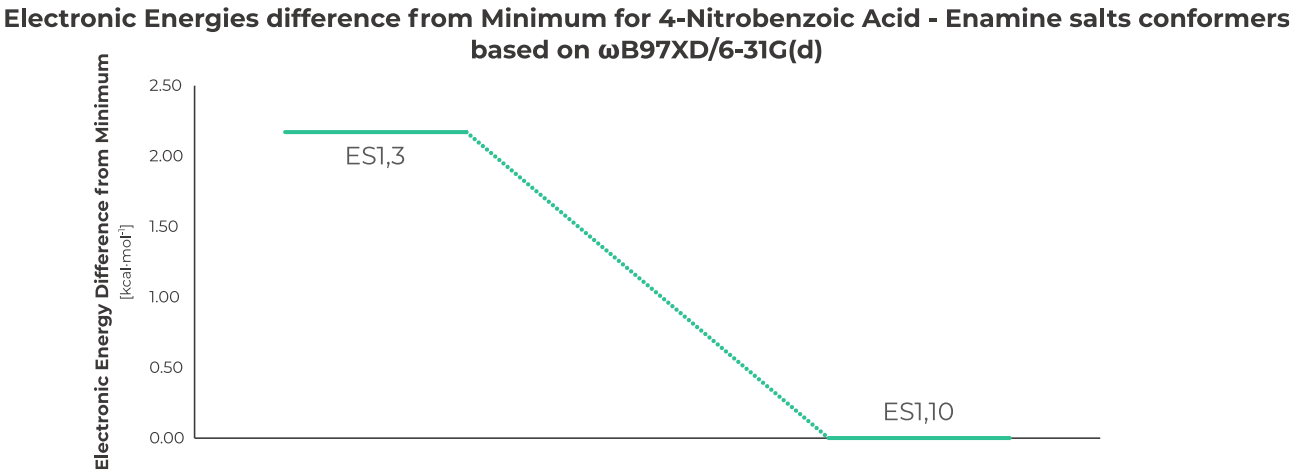

Figure 4.16 Electronic energy difference from global minimum for enamine–acid complex conformers.

From the last plot, it is possible to notice that the last DFT minimization led to an unexpected result. In particular, the protonation of the nitrogen atom causes a stabilization in energy for the enamine–acid complex conformer which is based on the *syn*–Me–*syn*–open enamine conformer *E1,10.* This has not been highlighted as the lowest energy conformation in section 4.3. An explanation to this surprising outcome can be given by looking at the

structure of the two conformers reported in figure 4.17. In particular, it is possible to see that it is precisely due to the relative disposition of the methoxyquinolinic respect to the quinuclidinic cage which generates the *syn*–open conformation. In *ES1,10* structure, this conformation comes with the *syn* relative disposition of the methyl group respect to the quinuclidine moiety. These two factors promote the instauration of a 2.73 Å long hydrogen–bonding interaction between the oxygen atom of the organic carboxylate and the hydrogen atom of the abovementioned methyl group.

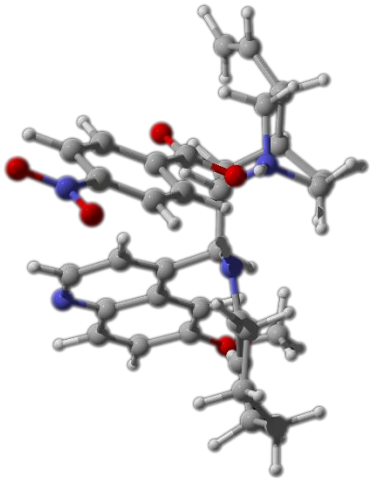

anti–closed enamine salt conformer

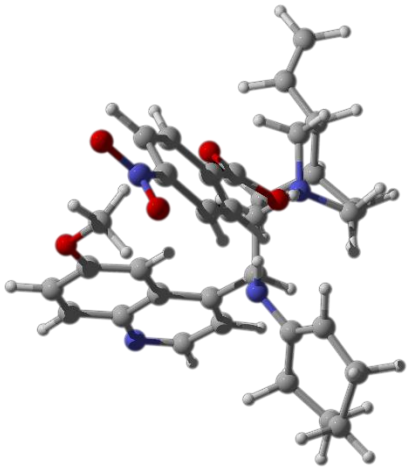

syn–Me–*syn*–closed enamine salt conformer

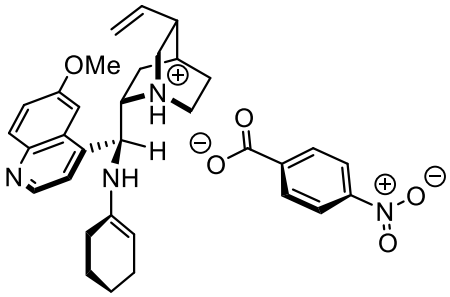

ES1,3 (A)

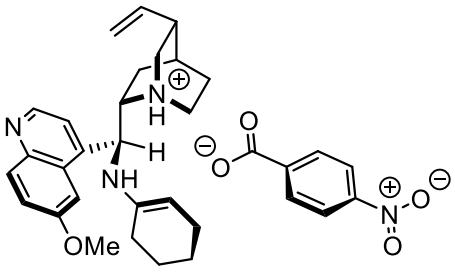

ES1,10 (B)

Figure 4.17. A: *Ball and stick* representation of *ES1,3* structure derived from quinine amine–derivative *anti*–open conformation; B: *Ball and stick* representation of *ES1,10* structure derived from quinine amine–derivative *syn*–Me–*syn*–open conformation.

Lastly, the Boltzmann distribution has been calculated both in vacuum and in condensed phase consisting in a toluene solution evaluated by exploiting the CPCM method.

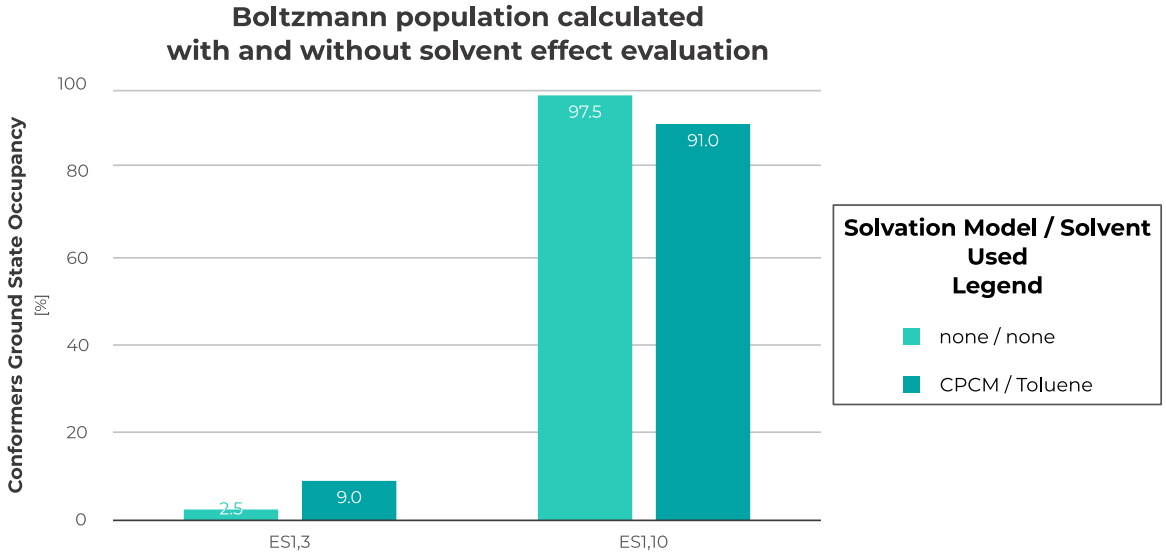

Figure 4.18. Comparison of Boltzmann distribution of enamine salt conformers calculated in vacuum (lightest green colour) and with the evaluation of toluene solvation effect (dark green).

4.5 Transition state structure DFT optimization

Once the ground state conformers of both enamine–acid complex and *trans*–β–nitrostyrene have been obtained, all the building–blocks for the research of the energetically favoured transition state geometries are present.

4.5.1 Relaxed scan and constrained DFT optimization

First of all, it has been necessary to find the energy profile for the formation of the bond between the two reaction centres. The Michael addition reaction allows for the formation of a carbon–carbon bond between a nucleophile carbon double bond and an electrophilic carbon atom.

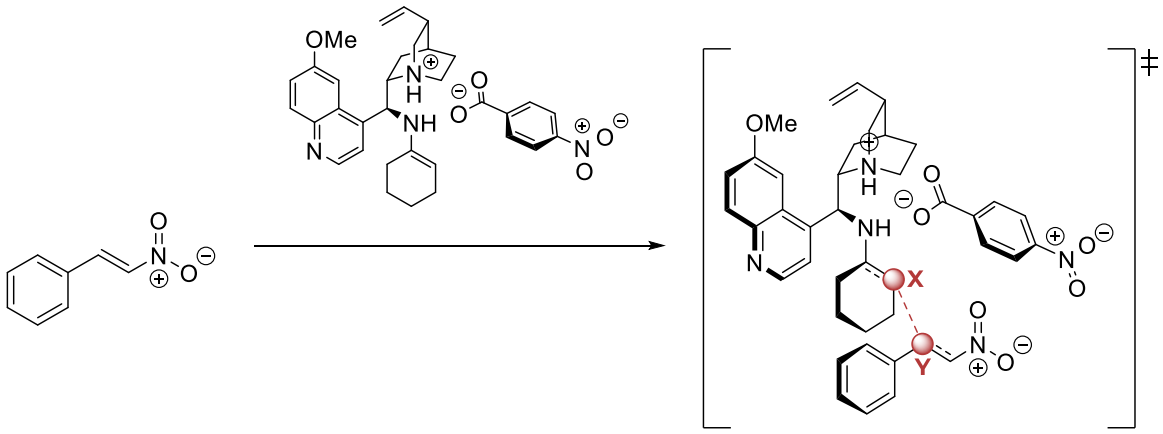

Figure 4.19 Transition state geometry for one possible combination of prochiral faces.

To obtain the transition state geometry, a relaxed potential energy surface (PES) scan was initially performed by progressively approaching the two reactive atoms (red balls in figure 4.19): the carbon in α–position of the enamine and the one in β–position to the nitro moiety to the *trans*–β–nitrostyrene. A relaxed scan consists of a series of calculations (steps) in which one of the structural parameters (in our case the X–Y bond distance) is fixed to a certain value, while all other parameters are optimized to their most favourable values. Prior to each step of the scan the fixed parameter is varied according to a series of predetermined values. An example of the result of this calculation is presented in figure 4.20, which shows the result of the relaxed scan involving the X–Y bond distance which was scanned between the initial value of 2.48 Å and the final value of 1.33 Å in 23 steps with 0.05 Å increments.

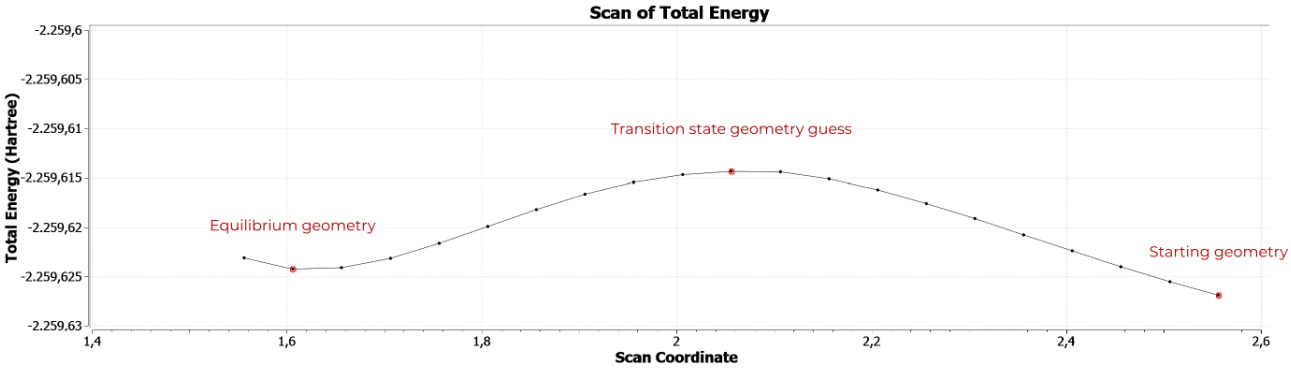

Figure 4.20. Example of the plot resulting from an approaching scan.

This plot relates the electronic energy associated to the whole system to the distance between the two reaction centres involved, namely the scan coordinates. It is evident that the plot present two critical points, a minimum and a maximum. The minimum corresponds to the energy associated to the equilibrium length of the bond between the two atoms of the initially isolated molecule while the maximum corresponds to the transition state for the two molecules in the system.

In this scenario, the approach of every *trans*–β–nitrostyrene prochiral face to both enamine salt conformers has been computed with a ωB97X–D/6–31G(d) DFT calculation in 25 steps in which the reaction centres are brought up by 0.05 Å and the geometry

The distances between the reaction centres in the transition state geometries associated to the maximum in the relaxed scan plot for all the four possible faces superimposition for both the enamine salt conformers are reported in table 4.3. To ensure the most rigorous representation of all the transition state geometries, not only the structure associated to the energy maximum but also the two nearby structure with lowest energy have been taken in consideration for the calculation.

Table 4.3. Reaction centres distance calculated for every prochiral faces superimposition.

	Major enamine salt conformer *E1,10*	**Minor enamine salt conformer** *E1,3*
Prochiral Faces	**Reaction centres distances** [Å]	
Re–Re	2.10 ± 0.05	2.03 ± 0.05
Si–Si	1.99 ± 0.05	2.10 ± 0.05
Re–Si	1.85 ± 0.05	1.97 ± 0.05
Si–Re	1.97 ± 0.05	2.06 ± 0.05

All the 24 geometries have been further optimized with another ωB97XD/6–31 G(d) DFT calculation keeping the distances found during the scan fixed. At the end of this two–steps procedure, the resulting geometries can be considered quite close to the effective transition state geometry.

4.5.2 Transition states DFT optimization guided by Berny algorithm

Final ωB97XD/6–31G(d) DFT calculations have been carried out to optimize all the 24 abovementioned geometries to their corresponding transition states through the Berny algorithm. This algorithm initially developed by Bernhard Schegel is nothing but a minimization algorithm which forces the second derivative matrix to contain a single negative eigenvalue. Obtaining a single negative eigenvalue is crucial since it discriminates among first order saddle points to others critical points on the potential energy surface.

The results in the application of such optimization algorithm with also the evaluation of the toluene solvation effect based on CPCM model suggested the existence of three possible transition state geometries characteristic to each single facial superimposition, which are reported in table 4.4. By looking at the table is clear that for both of the enamine salt

conformers the energetically favoured transition state is the one resulting by the reaction on its *Re* prochiral face with the *trans*–β–nitrostyrene *Re* prochiral face.

Table 4.4. Summary of bond length and relative electronic energies for transition state.

	Major enamine salt conformer *E1,10*		**Minor enamine salt conformer** *E1,3*	
Prochiral Faces	**Average Bond Length** [Å]	**Δ E from absolute minimum** [kcal·mol^{-1}]	**Average Bond Length** [Å]	**Δ E from absolute minimum** [kcal·mol^{-1}]
Re–Re	2.14	0.00	2.10	0.00
Si–Si	2.06	3.62	2.11	3.23
Re–Si	2.04	14.79	1.99	4.05
Si–Re	2.02	1.39	2.11	7.29

Then the Boltzmann distribution characteristic of each set of transition states has been calculated and then corrected on the basis of the statistical distribution of enamine salt conformers in order to obtain the single distribution reported in figure 4.21.

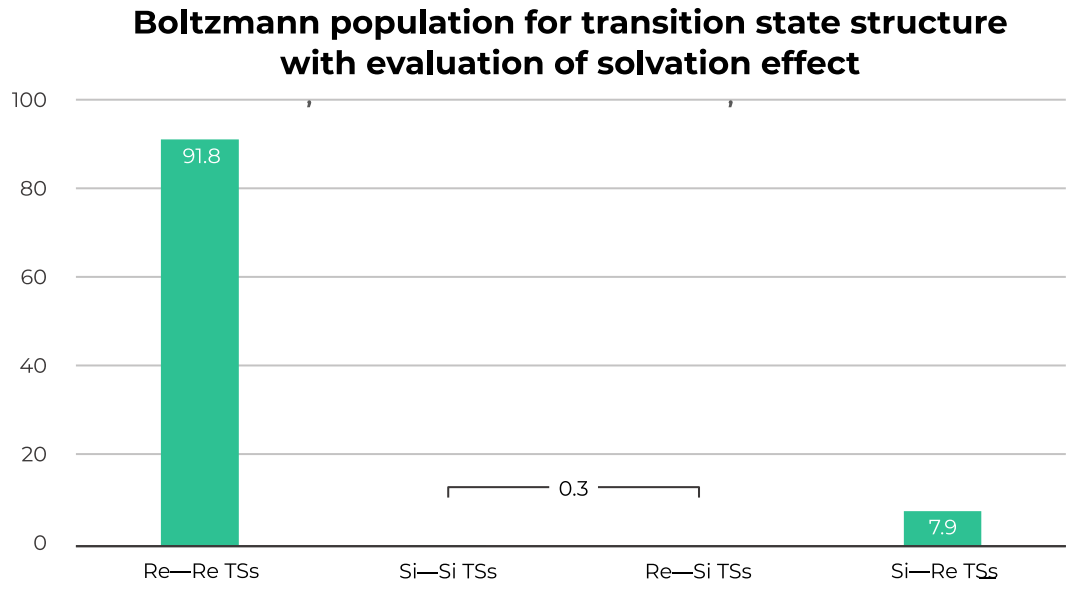

Figure 4.21. Boltzmann population distribution of transition state structures.

The abovementioned distribution can be used as a projection of the diasteromeric ratio for the reaction by looking at the transition state three–dimensional structures obtained to extrapolate the single diastereoisomer structures. The transition state generated from the reaction on the *Re* prochiral face of both reagents is represented in figure 4.22. It is possible to rationalize this transition state trough a *syn*–clinal model in which the empty orbital of the positive charged nitrogen atom which belongs to the *trans*–β–nitrostyrene is perpendicular to the lone electron pair characteristic of the enamine nitrogen atom. In this context the two orbitals interact by retro–donation causing a strong stabilization of the structure. This could be the reason why this particular transition state is the most energetically favoured. However, it is possible to observe that this transition state is the one which product a *syn* diasteroisomer.

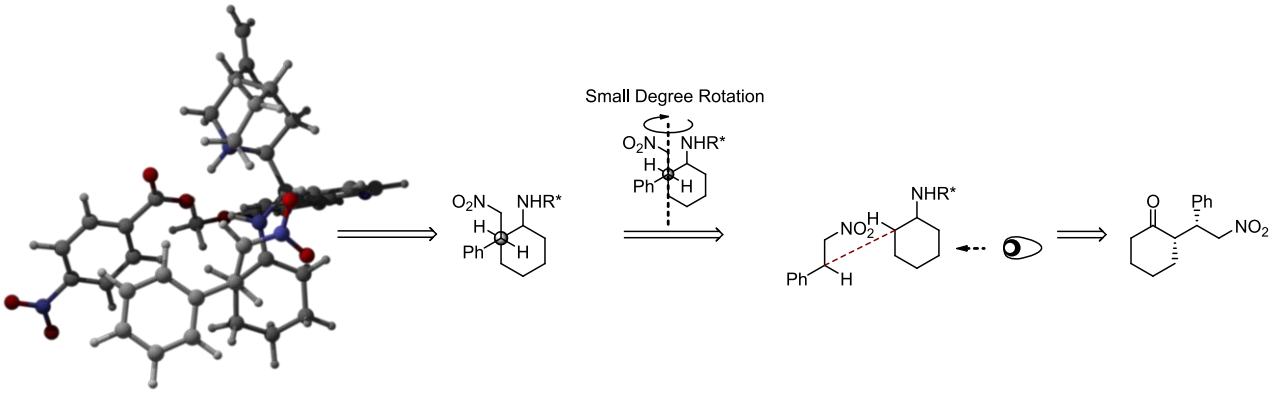

Figure 4.22. *Ball and stick* representation of transition state structure obtained from the reaction onto both *ES1,10* and *trans*–β–nitrostyrene *Re* prochiral faces.

In figure 4.23 it is indeed reported the transition state generated from the reaction on the enamine *Si* prochiral face and the *trans*–β–nitrostyrene *Re* prochiral face. Here it is possible to observe that this transition state is the one which product an *anti* diasteroisomer.

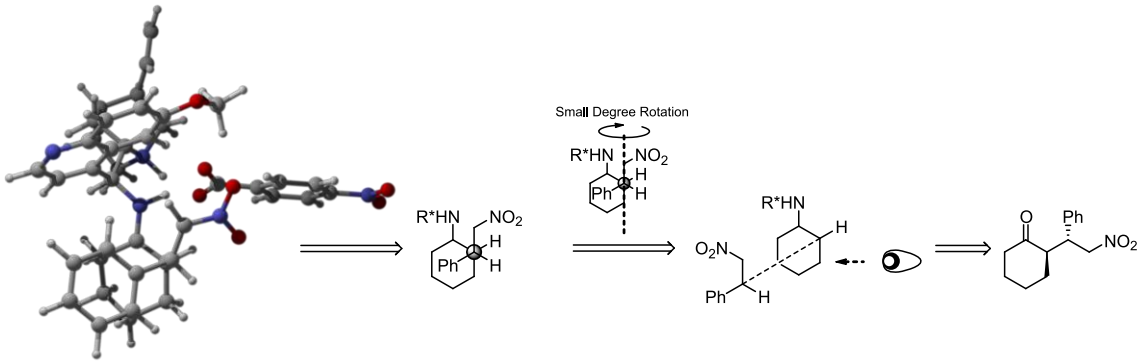

Figure 4.23 *Ball and stick* representation of transition state structure obtained from the reaction between *ES1,3* prochiral *Si* face and *trans*–β–nitrostyrene prochiral *Re* face.

Professor Ciogli and professor Villani group have derived an experimental *syn*:*anti* diasteromeric ratio equal to 88:12, while the Boltzmann distribution reported in figure 4.17 suggests a *syn*:*anti* diasteromeric ratio equal to 92:8. The results are in agreement under the experimental error suggesting that the computational route adopted until now can be improved but it is all in all reliable.

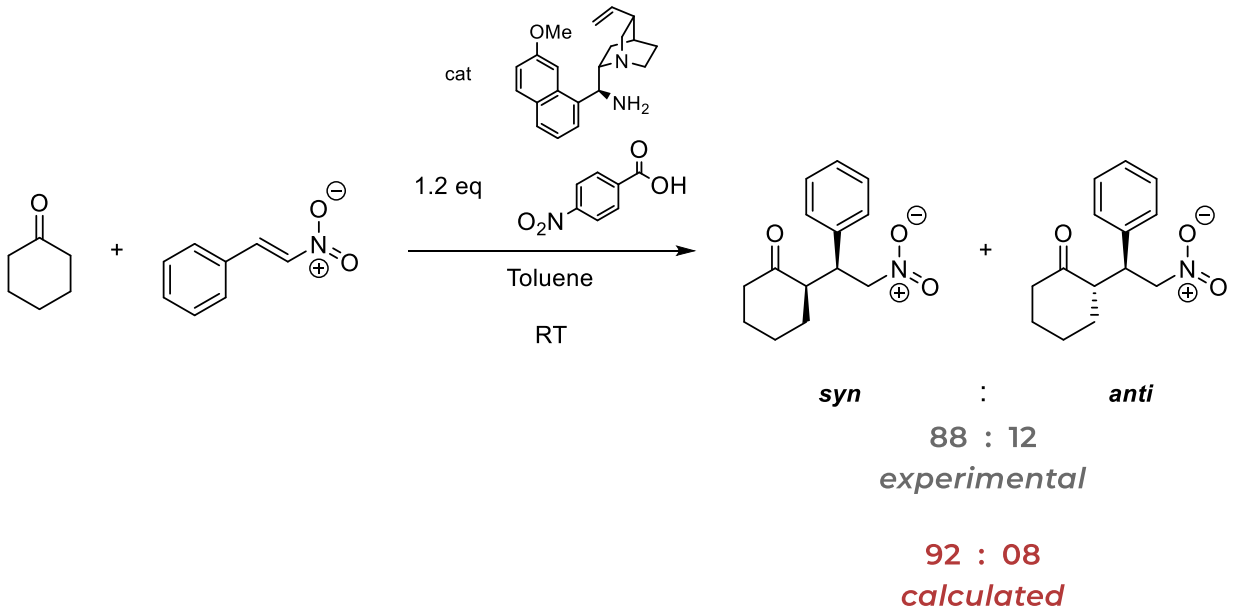

Figure 4.24. Comparison between the calculated and experimental obtained diasteromeric ratio for the Michael addition of cyclohexanone to *trans*–β–nitrostyrene catalysed by 9–*epi*–9–amino–9–deoxyquinine and 4–nitrobenzoic acid.

At this point, the computational strategy has been started over in order to evaluate the effect of another organic acid cocatalyst on the same reaction, in particular the 4–hydroxy–benzoic acid.

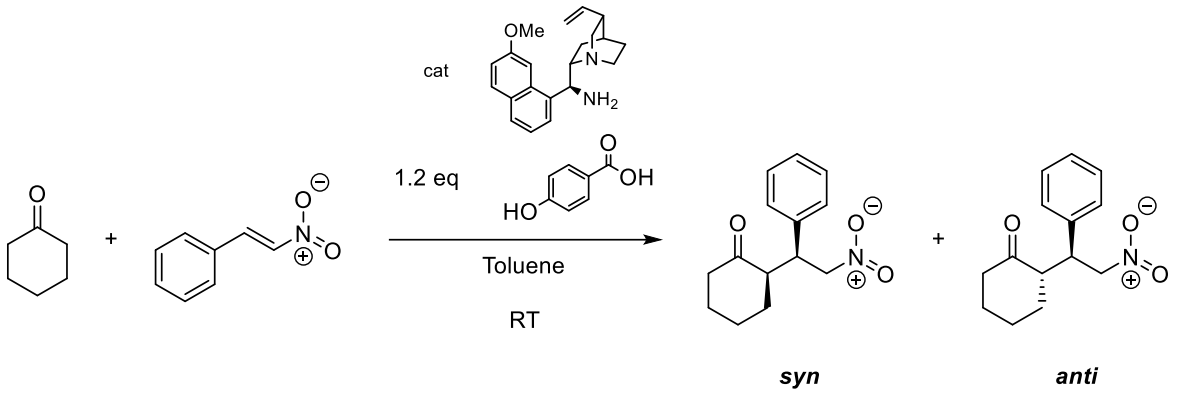

Figure 4.25. Michael addition of cyclohexanone to trans–β–nitrostyrene catalysed by 9–epi–9–amino–9–deoxyquinine and 4–hydroxybenzoic acid.

4.6 Conformational analysis of the 4–hydroxybenzoic acid

Following the same procedure highlighted in section 4.1, the conformational space relative to the 4–hydroxy–benzoic acid has been evaluated unearthing two low energy conformers reported in figure 4.26.

4–HBA–180 **4–HBA–0**

Figure 4.26. The two conformers of differentiated by a 180–degree rotation of the "H – O – C_{OH} – C_α" dihedral.

From their structure it is possible to see that they differ uniquely for the rotation of the dihedral angle identified by the hydroxyl moiety atoms, the carbon atom bonded with the oxygen and the carbon atom in α–position to this last one (H – O – C_{OH} – C_α in figure 4.21): for these reason the two conformer will be reported with the *4–HBA* acronym stands for 4–hydroxy–benzoic acid and the following integer number represent the rotation of the abovementioned dihedral angle.

In the study of Cesari *et al.*[8] on phenol lowest energy conformers, it has been outlined that the two energetically favoured phenol conformation are distinguished by a 180–degree rotation of the abovementioned dihedral angle. Even if the hereby structure under analysis is not phenol, it can be considered its *para*–substituted derivative. Moreover, has been observed in section 4.1 that the carboxylic moiety has zero degrees of dihedral rotation. For this reason, the 4–hydroxy–benzoic acid conformational space has been assumed almost congruent to the phenol one.

4.7 DFT optimization of 4–hydroxybenzoic acid conformers

The optimization to a minimum of the abovementioned conformers has been carried out with a ωB97X–D/6–31G(d) based DFT calculation and the resulting Boltzmann distribution is reported in figure 4.27.

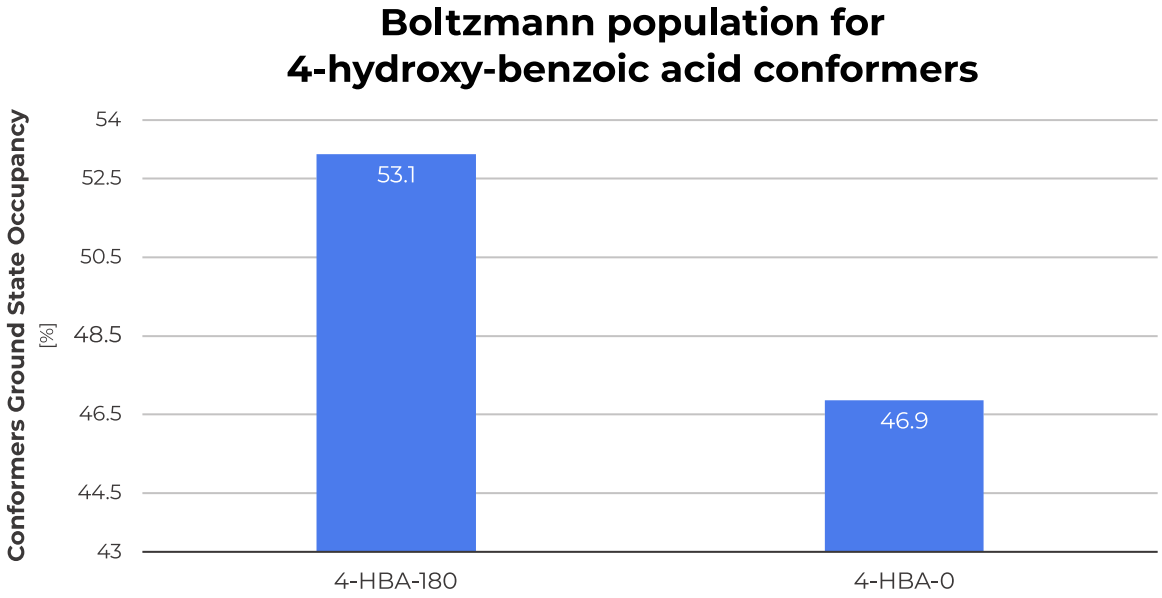

Figure 4.27. Boltzmann distribution of 4–hydroxybenzoic acid conformers.

As predictable, neither conformers converged into the other one and moreover, they occupy the ground state in almost equal quantity. As a consequence of the obtained results, both conformers must be used in the construction of the enamine salts.

Moreover, these results can be considered reliable since they are in line with the results obtained by Cesari and coworkers on phenol, used in this context as a model.

4.8 DFT optimization of enamine–4–hydroxybenzoic acid complex conformers

The enamine salt conformers have been constructed following the same insights proposed in section 4.4 but also the same hybrid functional and basis set. Starting from the enamine conformers *E1,3* and *E1,10* previously found, two set of enamine salt conformers have been constructed as two acid conformers has been found. Different optimizations to a minimum of the system have been carried out in order to evaluate the electronic energy of many conformers differentiated by slight rotation in space of the acid structure nearby the quinuclidine nitrogen atom. The results for both set of conformers are reported in figure 4.28.

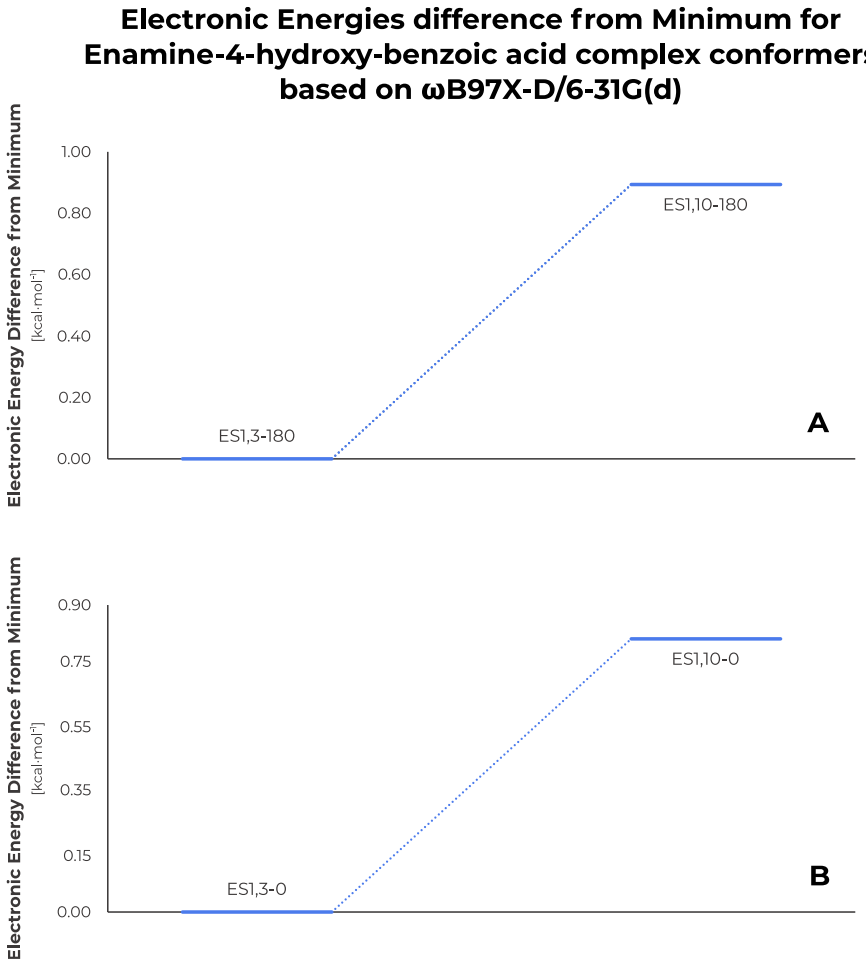

Figure 4.28. A: electronic energy difference from global minimum for enamine–4–hydroxy–benzoic acid–180 conformers. B: electronic energy difference from global minimum for enamine–4–hydroxy–benzoic acid–0 conformers.

These optimizations led to a different result if compared to the enamine–4–nitro–benzoic acid complex conformers. In particular, the enamine salts formed with both 4–hydroxy–benxoic acid conformers show as energetically favoured conformation the one deriving from the *anti*–open enamine conformer. A clearer visualization of this separation is reported in figure 4.29 where the Boltzmann distribution for both set of conformers are reported after the evaluation of the toluene solvation affect trough the CPCM model.

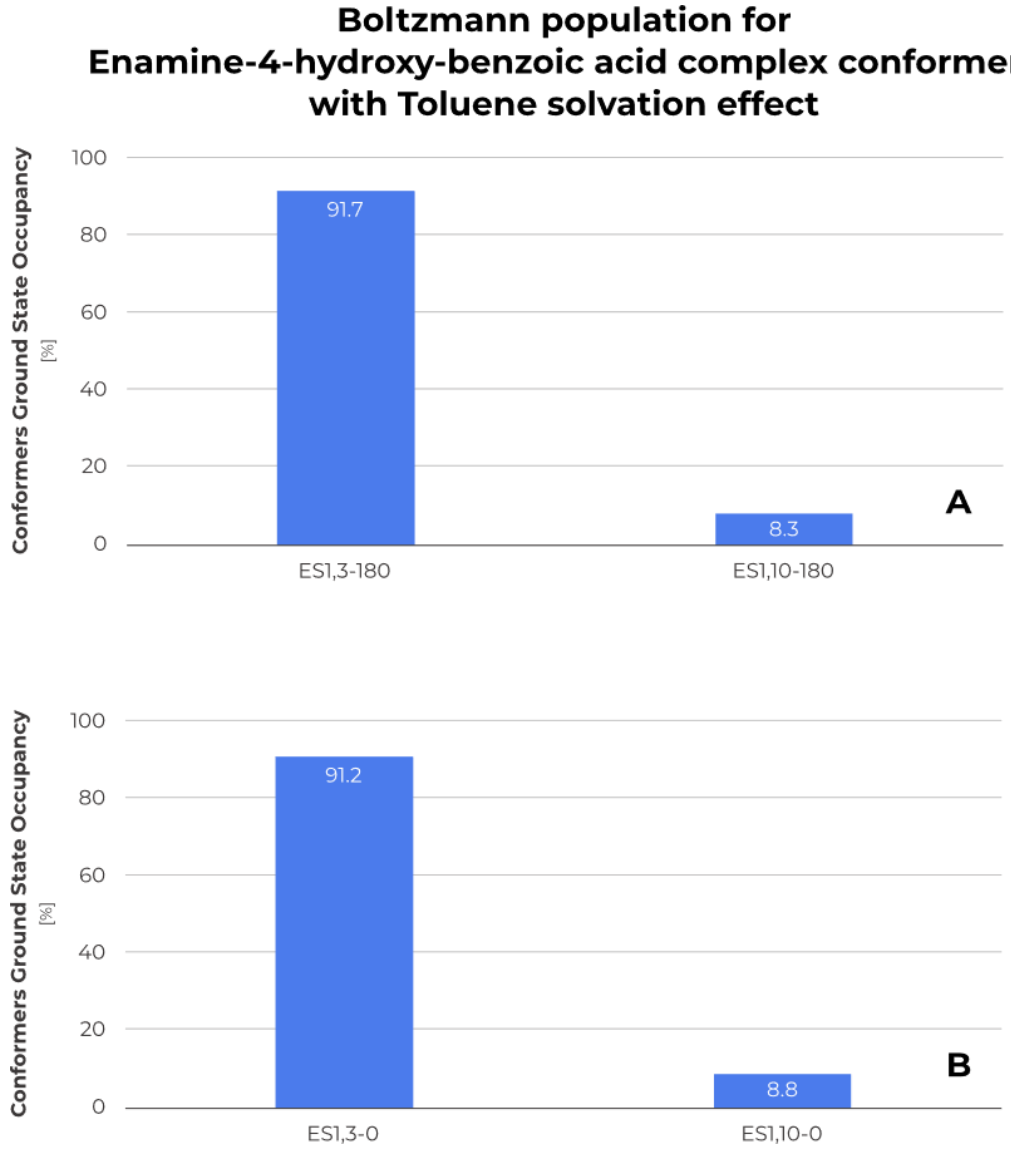

Figure 4.29. A: Boltzmann distribution of enamine–4–hydroxy–benzoic acid–180 conformers. B: Boltzmann distribution of enamine–4–hydroxy–benzoic acid–0 conformers.

As an example, it is possible to notice by looking at the structure of the two conformers enamine salts conformers derived from the introduction of conformer 1 of 4–hydroxy–benzoic acid (figure 4.30), that they are quite similar to their 4–nitrobenzoic acid derived counterpart.

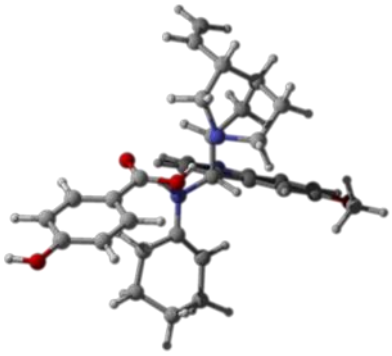

ES1,3–180°

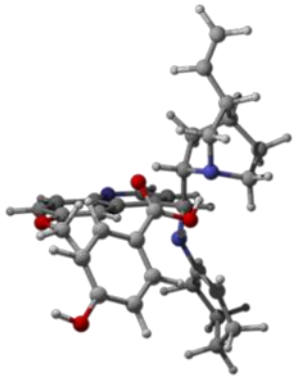

ES1,10–180°

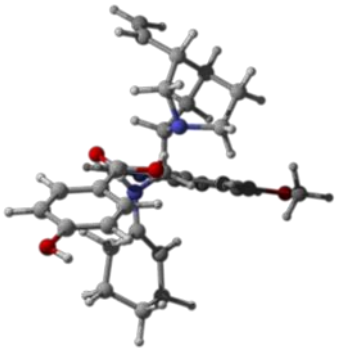

ES1,3–0°

anti–closed enamine salt conformer

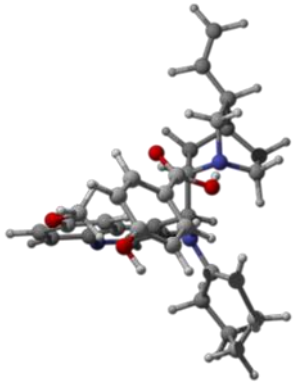

ES1,10–0°

syn–Me–*syn*–closed enamine salt conformer

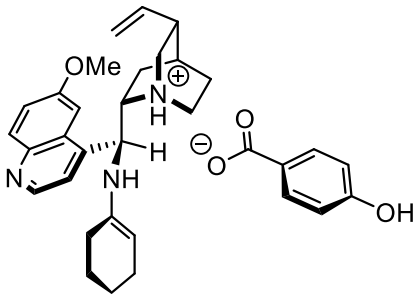

ES1,3–0° / 180° (A)

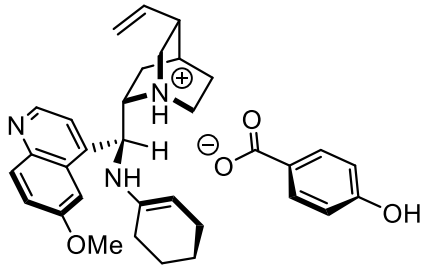

ES1,10–0° / 180° (B)

Figure 4.30. A: *Ball and stick* representation of *ES1,3–180* and *ES1,3–0* structure derived from quinine amine–derivative *anti*–open conformation; B: *Ball and stick* representation of *ES1,10–180* and *ES1,10–0* structure derived from quinine amine–derivative *syn*–Me–*syn*–open conformation.

It is possible to highlight that in the minor conformer the distance between the oxygen and hydrogen atoms which were supposed to weakly interact lowering the energy of the *syn*–open enamine conformer is longer than the outlined in section 4.4.3. For this reason, it has been hypnotised that in this scenario the repulsive forces are not sufficiently balanced by this weak interaction to allow the stabilization of the *syn*–open conformer–derived salt.

4.9 Transition state structure DFT optimization

As the ground state enamine–acid complex conformers have been obtained, a relaxed scan optimization between these last ones and *trans*–β–nitrostyrene has been carried out on all the prochiral faces following the procedure highlighted in section 4.5. The distances between the reaction centres in the three possible transition state geometries considered for all the four possible faces superimposition for all the four enamine salt conformers are reported in table 4.5.

Table 4.5. Reaction centres distance calculated for every prochiral faces superimposition.

Based on 4–hydroxybenzoic acid conformer 180°		
	Minor enamine salt conformer *E1,3–180*	**Major enamine salt conformer** *E1,10–180*
Prochiral Faces	**Reaction centres distances** [Å]	
Re–Re	2.06 ± 0.05	1.84 ± 0.05
Si–Si	2.08 ± 0.05	2.06 ± 0.05
Re–Si	1.91 ± 0.05	2.03 ± 0.05
Si–Re	2.04 ± 0.05	2.01 ± 0.05

Based on 4–hydroxybenzoic acid conformer 0°		
	Major enamine salt conformer *E1,3–0*	**Minor enamine salt conformer** *E1,10–0*
Prochiral Faces	**Reaction centres distances** [Å]	
Re–Re	2.04 ± 0.05	1.86 ± 0.05
Si–Si	2.05 ± 0.05	2.01 ± 0.05
Re–Si	1.95 ± 0.05	2.00 ± 0.05
Si–Re	2.06 ± 0.05	2.02 ± 0.05

All the 48 geometries have been further optimized with a ωB97XD/6–31 G(d) based DFT calculation keeping the above reported distances fixed.

4.9.1 Transition states DFT optimization guided by Berny algorithm

Final ωB97XD/6–31G(d) DFT calculations have been carried out to optimize all the 48 abovementioned geometries to their corresponding transition states through the Berny algorithm with also the evaluation of the toluene solvation effect based on CPCM model. By looking at the table is clear that for both of the enamine salt conformers the energetically favoured transition state is the one resulting by the reaction on its *Re* prochiral face with the *trans*–β–nitrostyrene *Re* prochiral face. The results of this last optimization procedure are reported in table 4.6.

Table 4.6. Summary of bond length and relative electronic energies for transition state involving 4–hydorxy–benzoic acid.

Based on 4–hydroxybenzoic acid conformer 180°				
	Major enamine salt conformer *E1,3–180*		**Minor enamine salt conformer** *E1,10–180*	
Prochiral Faces	**Average Bond Length [Å]**	**Δ E from absolute minimum [kcal·mol^{-1}]**	**Average Bond Length [Å]**	**Δ E from absolute minimum [kcal·mol^{-1}]**
Re–Re	2.10	8.40	1.97	10.17
Si–Si	2.12	1.24	2.13	9.26
Re–Si	1.99	12.13	2.07	5.54
Si–Re	2.12	0.00	2.09	0.00
Based on 4–hydroxybenzoic acid conformer 0°				
	Major enamine salt conformer *E1,3–0*		**Mainor enamine salt conformer** *E1,10–0*	
Prochiral Faces	**Average Bond Length [Å]**	**Δ E from absolute minimum [kcal·mol^{-1}]**	**Average Bond Length [Å]**	**Δ E from absolute minimum [kcal·mol^{-1}]**
Re–Re	2.10	7.16	1.98	5.97
Si–Si	2.12	0.00	2.07	0.00
Re–Si	1.99	10.92	2.07	1.84
Si–Re	2.11	1.15	2.05	11.95

From the table 4.6 it is clear that two opposite situations arise from the two set of transition state conformers. For what concern the transition state based on the enamine–4–hydroxy–benzoic acid–180° complex conformers the lowest energy transition state geometry is the one generated by reaction on the *Si* enamine prochiral face and *Re trans*–β–nitrostyrene one. The second energetically favorite transition state geometry for the same set of conformers is the one generated by the reaction on the *Si* prochiral face for both the species involved. On

the other hand, the transition state which include the reaction on the *Si* prochiral face for both enamine and *trans*–β–nitrostyrene is the energetically favored for what concern the transition state based on the enamine–4–hydroxy–benzoic acid–0° complex conformers. The transition state geometry generated by reaction on the *Re*–*Si* prochiral faces of the enamine and *trans*–β–nitrostyrene, respectively, is the second energetically favored. The structure of the four abovementioned transition state both based on the major enamine salt conformer of the set, are reported in figure 4.31 and figure 4.32. It is possible to observe that the transition state geometries reported figure 4.31 in which the 4–hydroxy–benzoic–acid–180° conformer is present product an *anti* diasteroisomer and a syn diasteroisomer respectively.

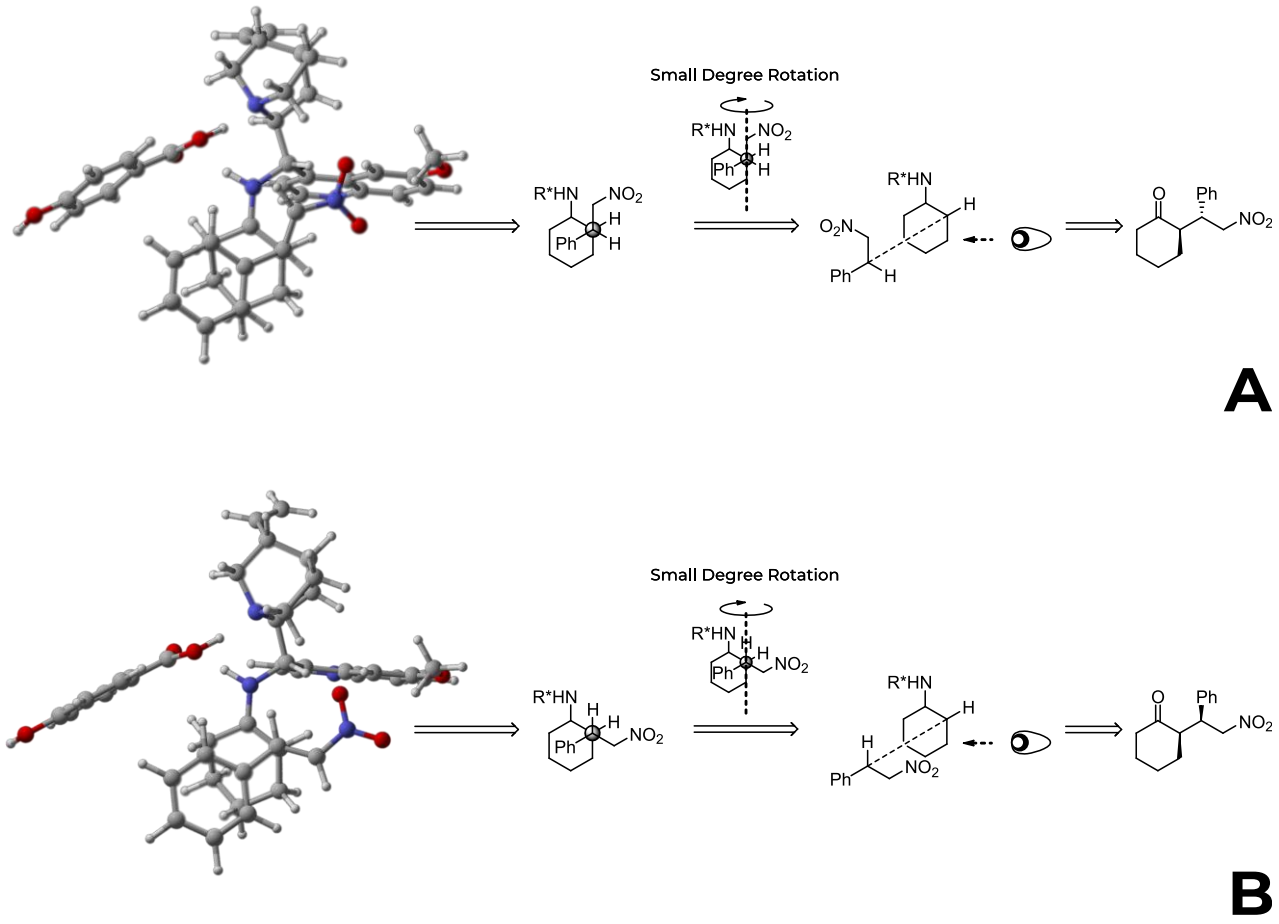

Figure 4.31. A: Ball and stick representation of the transition state structure calculated for the reaction onto ES1,3–180 *Re* prochiral face and trans–β–nitrostyrene *Si* prochiral faces.

B: *Ball and stick* representation of the transition state structure calculated for the reaction onto both *ES1,3–180* and *trans*–β–nitrostyrene *Si* prochiral faces.

An analog situation is reported figure 4.32 in which can be observed that the products generated by the transition state geometries in which the 4–hydroxy–benzoic–acid–0° conformer is involved are the same.

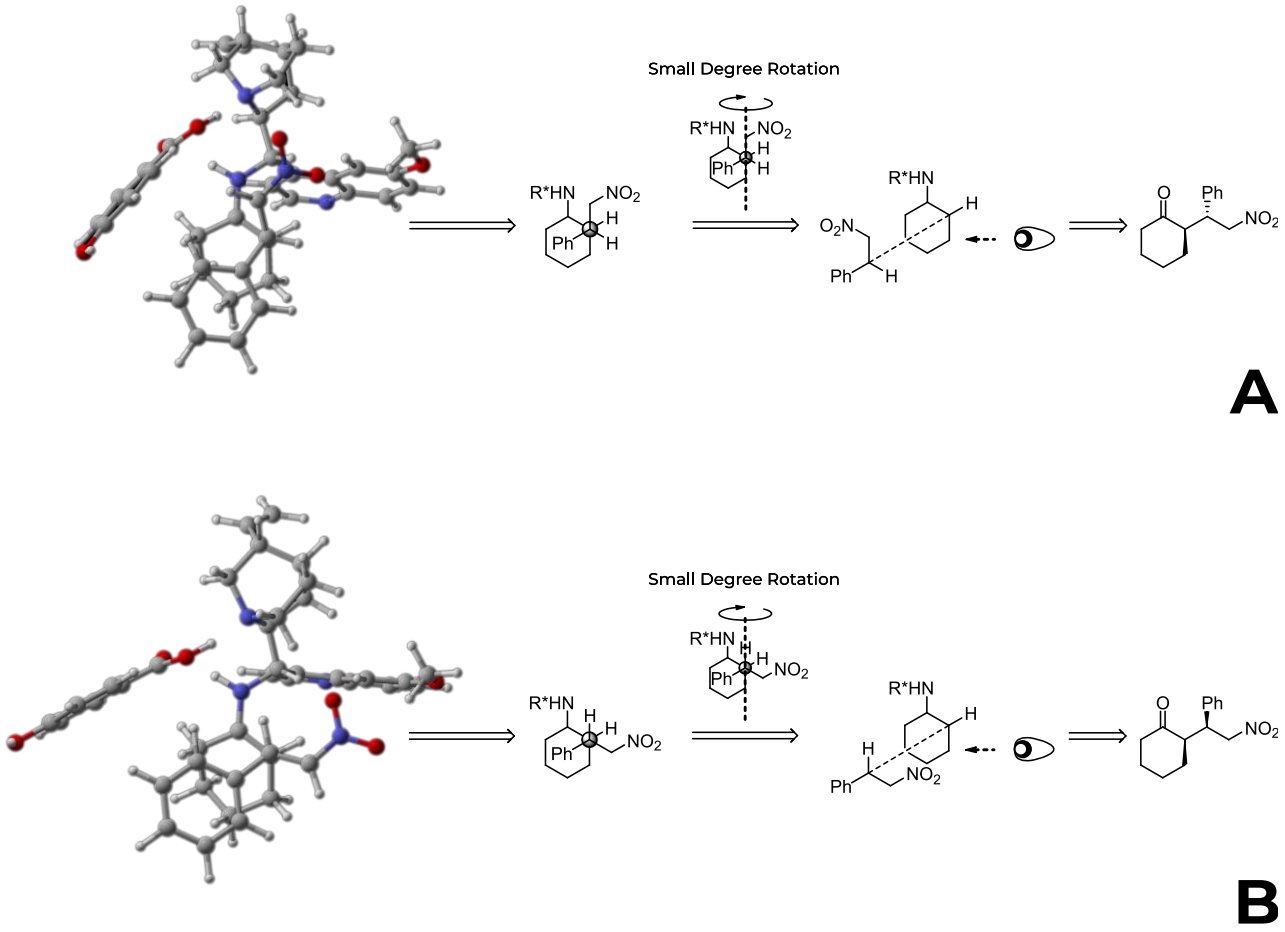

Figure 4.32. A: Ball and stick representation of transition state structure obtained from the reaction onto ES1,3–0 *Re* prochiral face and trans–β–nitrostyrene *Si* prochiral faces.

B: *Ball and stick* representation of transition state structure obtained from the reaction onto both *ES1,3–0* and *trans*–β–nitrostyrene *Si* prochiral faces.

However, it is possible to notice from the individual Boltzmann distribution (figure 4.33) calculated for both the set of conformers with the corrections based on the two previous calculated distribution of the two set of enamine salt conformers that the diasteromeric ratio obtained is almost opposite in value.

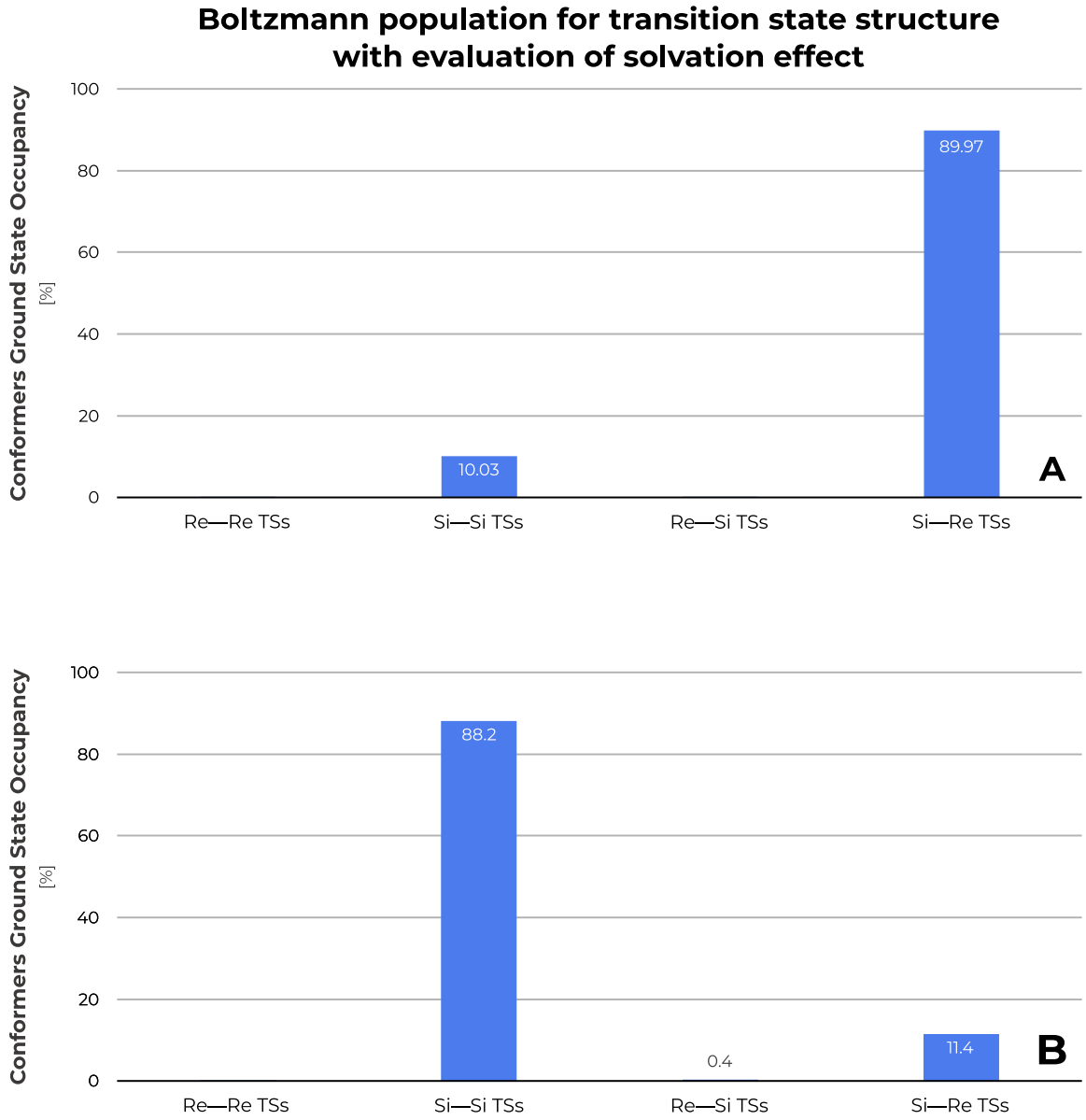

Figure 4.33. A: Boltzmann distribution of transition state structures derived from enamine–4–hydroxy–benzoic acid–180 conformers.

B: Boltzmann distribution of transition state structures derived from enamine–4–hydroxy–benzoic acid–0 conformers.

Professor Ciogli and professor Villani group have derived in this case an experimental *syn*:*anti* diasteromeric ratio equal to 83:17. The Boltzmann distribution reported in figure 4.33B suggests a *syn*:*anti* diasteromeric ratio equal to 88:12. The result obtained exploiting the enamine–4–hydroxy–benzoic acid–0° conformer is in agreement but over the experimental error by 1%. Unlike the case illustrated at the end of section 4.5.2, it is not possible to affirm that the computational route adopted is reliable since the diasteromeric ratio obtained exploiting the enamine–4–hydroxy–benzoic acid–180° conformer is opposite to the experimental result obtained. In this scenario many differ factor could affect the final result, in particular it has been accounted to a human error in reading the scan plot resulting from the approaching scan.

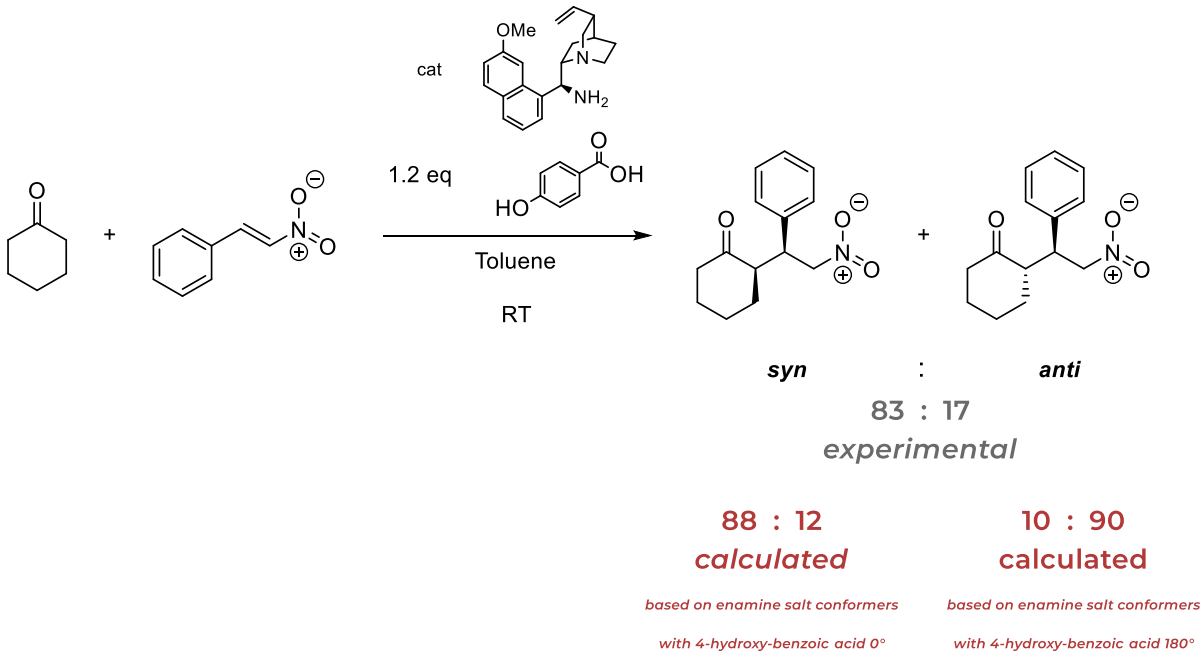

Figure 4.34. Comparison between the calculated and experimental diasteromeric ratio for the Michael addition of cyclohexanone to *trans*–β–nitrostyrene catalysed by 9–*epi*–9–amino–9–deoxyquinine and 4–hydroxy–benzoic acid.

4.10 Comparison of the results obtained with the two acids

The results obtained in the study of the 4–nitro–benzoic acid cocatalysed Michael addition are in agreement with the experimental results. It is not possible to say the same for what concern the 4–hydroxy–benzoic acid cocatalysed reaction. Even if one set of conformers has shown good agreement to the experimental results, the other one showed an opposite disteroselectivity in comparison to the one experimentally observed. Focusing our attention on the results which best approximate the experimental observations, the two acids studied give rise to two different major transition states which are responsible for the formation of the two enantiomers constituting the *syn*–diasteroisomers.

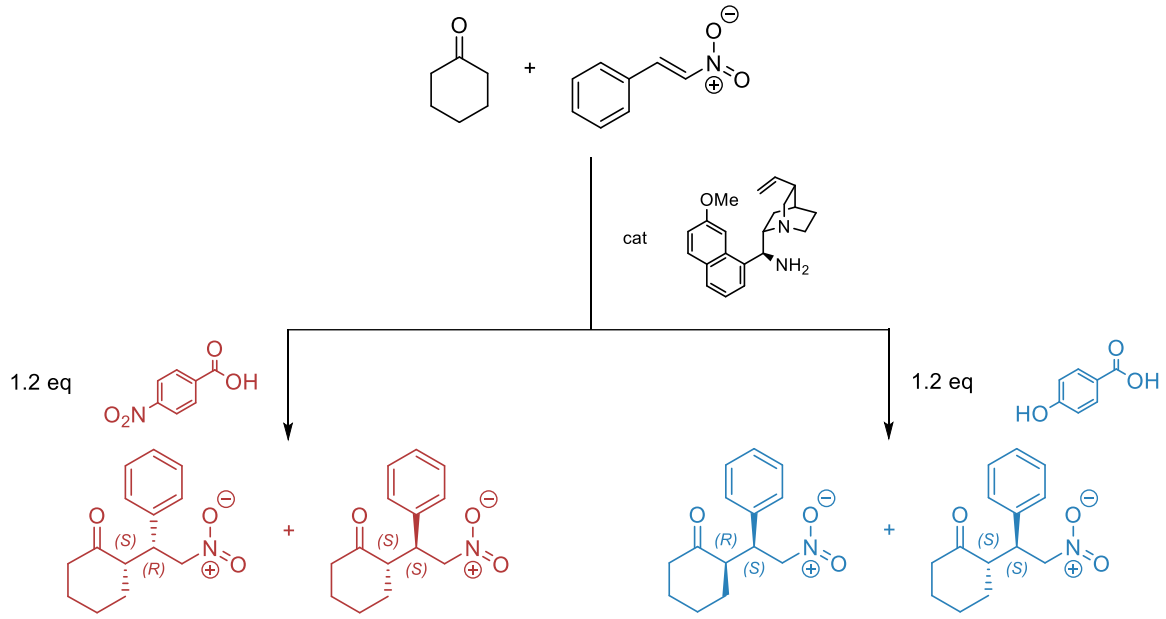

Figure 4.35. Comparison of the single enantiomers obtained by the calculation based on 4–nitro–benzoic acid (in red) and 4–hydroxy–benzoic acid 0° conformer (in blue).

However, it is also possible to see in figure 4.35 that the same enantiomer of the *anti*–diasteroisomer is obtained for both the reacting system.

Finally, it is possible to analyse the difference in electronic energy between the two energetically favoured transition states based on the major enamine salt conformer of each acid cocatalyst. In figure 4.36 is reported the difference between the transition state structure

generated by the reaction on both *Re* prochiral faces when the enamine–4–nitro–benzoic acid complex is present in the reacting system and the transition state structure generated by the reaction on both *Si* prochiral faces when the enamine–4–hydroxy–benzoic acid 0° conformer complex is involved. The minimum in electronic energy is hereby represented by the *trans*–β–nitrostyrene and enamine salt major conformer optimized in the same system.

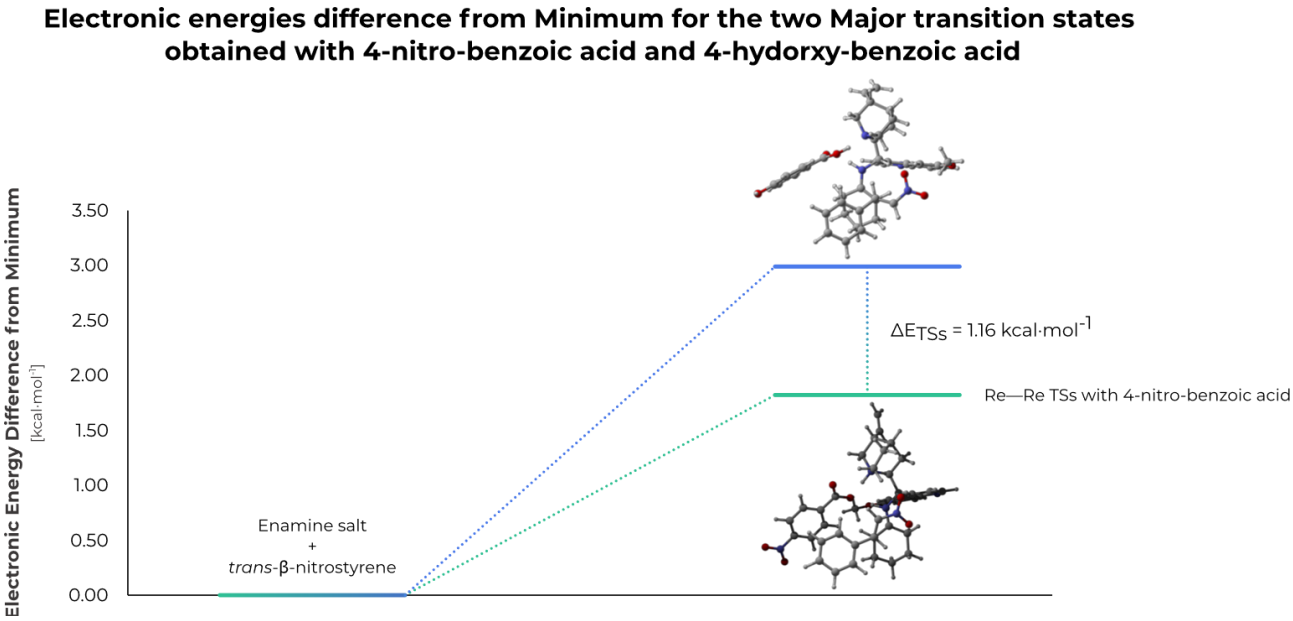

Figure 4.36 A: electronic energy difference from global minimum for both 4–nitro–benzoic acid based and 4–hydroxy–benzoic acid–0 conformer based transition states.

Professor Ciogli and professor Villani group have highlighted that after 48 hour, the concentration of the product relative to the reaction which involves the 4–nitro–benzoic acid is significantly higher in comparison to the reaction conducted with 4–hydroxy–benzoic acid as cocatalyst. This difference in reactivity can be explained by the 1.16 kcal·mol^{-1} which separates the two transition states. As a matter of fact, the reagent has to overcome a smaller energy barrier to assume the transition state geometry in the reaction which involves the 4–nitro–benzoic acid.

4.11 References

1. Willoughby, P. H., Jansma, M. J. & Hoye, T. R. A guide to small–molecule structure assignment through computation of (1 H and 13 C) NMR chemical shifts. *Nat. Protoc.* 9, 643–660 (2014).

2. Allinger, N. L., Allinger, J. & DaRooge, M. A. Conformational Analysis. XXXVIII. The Conformations of Cyclohexanone Rings. 86, 4061–4067 (1964).

3. Frisch, M. J.; Trucks, G. W.; Schlegel, H. B.; Scuseria, G. E.; Robb, M. A.; Cheeseman, J. R.; Scalmani, G.; Barone, V.; Petersson, G. A.; Nakatsuji, H.; Li, X.; Caricato, M.; Marenich, A. V.; Bloino, J.; Janesko, B. G.; Gomperts, R.; Mennucci, B.; Hratch, D. J. Gaussian 16, Revision 16.

4. Foresman, J. B. & Frisch, Æ. *Exploring chemistry with electronic structure methods. Gaussian Inc, Pittsburgh, PA* (2015).

5. Vayner, G., Houk, K. N. & Sun, Y. K. Origins of Enantioselectivity in Reductions of Ketones on Cinchona Alkaloid Modified Platinum. *J. Am. Chem. Soc.* 126, 199–203 (2004).

6. Moran, A., Hamilton, A., Bo, C. & Melchiorre, P. A mechanistic rationale for the 9–amino(9–deoxy) epi cinchona alkaloids catalyzed asymmetric reactions via iminium ion activation of enones. *J. Am. Chem. Soc.* 135, 9091–9098 (2013).

7. Dennington, Roy; Keith, Todd A.; Millam, J. M. GaussView, Version 6.

8. Cesari, L., Canabady–Rochelle, L. & Mutelet, F. Computational study on the molecular conformations of phenolic compounds. *Struct. Chem.* 29, 179–194 (2018).

5. Conclusions

Asymmetric amino catalysis is as fascinating as useful to obtain reaction product with defined stereochemistry but some mechanism involved in the formation of the product are unclear.

Thanks to the computation strategy adopted it was possible to successfully reproduce the diasteromeric ratio experimentally measured in the primary amine–catalysed Michael addition of cyclohexanone to *trans*–β–nitrostyrene by 9–*epi*–9–amino–9–deoxyquinine with 4–nitro–benzoic acid as acidic cocatalyst. The reproduction of the diasteromeric ratio values under the experimental error suggested that a reasonable approximation of the transition state geometry has been found.

Inspired by the promising results, the same computational route has been applied to the same reaction with a different acid cocatalyst: the 4–hydroxy–benzoic acid. In this scenario, the computational route apparently failed in the reproduction of the diasteromeric ratio since one of the two set of conformers shows the almost the exact opposite value of the experimentally obtained disteromeric ratio. Probably the error is not to account to the computational strategy, but rather to a misreading in the approaching scan output geometries.

This error and the desire in reduce the difference in the computed and experimentally derived diasteromeric ratio values suggested an improvement in the method itself as a future objective. Moreover, at least the effect of another acid cocatalyst is under evaluation to clarify the diasteroselection mechanism involved in the formation of the rection products.